Page left intentionally blank.

Testing Optical Elements of the Wide-Field Phasing Testbed for the Giant Magellan Telescope

A senior thesis presented

by

Peyton Benac

to

The Department of Astronomy

in partial fulfillment of the requirements

for the degree of

Bachelor of Arts

in the subject of

Astrophysics & Physics

Harvard University

Cambridge, Massachusetts

March 2021

Thesis Advisor: Dr. Brian McLeod Peyton Benac

Testing Optical Elements of the Wide-Field Phasing Testbed for the Giant Magellan Telescope

Abstract

The upcoming Giant Magellan Telescope will utilize both a segmented primary and secondary mirror, but to achieve diffraction-limited imaging, the alignment of the mirror segments must be precisely maintained. This will be accomplished with an active optics system, using both a dispersed fringe sensor and a Shack-Hartmann wavefront sensor to measure wavefront aberrations and account for them in the mirrors' position and figure. To minimize risks in the development of this system, a telescope simulator, called the Wide-Field Phasing Testbed, is being developed that will demonstrate the required phasing. This thesis presents the preliminary tests that have been performed to demonstrate progress toward this eventual full testbed. We measure the tip-tilt and piston displacement errors of two mirror facets, and set constraints for the precision of the alignment procedure for a complex reflective system.

Contents

Acknowledgments

I am grateful to my patient and helpful advisor, Dr. Brian McLeod, as well as to the other members of the AGWS team, especially Jan Kansky for all his help with the data acquisition software, and Dan Catropa for his help with mechanical design of parts and systems. I am also grateful to the 2020-21 Astronomy 99 class and Professor John Kovac for their comments and suggestions throughout this project. Personally, I have been supported throughout this project by Kim and Tony Benac, Sam Benac, and Hamish Nicholson. I'd also like to thank my bike for taking me to and from the lab in Alewife to allow this thesis to come to fruition.

Additionally, some figures used in this thesis are reproduced from other sources. Sources are listed in the captions, but are listed here as well: GMT Organization (GMTO), 4DTechnology, the NOAO Active Optics Tutorial by A. Tokovinin, and internal SAO/GMTO documents like Kansky et al. (2020) and McLeod et al. (2021). Figures 3.8, 3.9, 3.10, 3.11, 3.12, 3.13, and 3.14 were reproduced from Dr. McLeod's slides from the WFPT Preliminary Design Review slideshow. Figures 2.23 and 2.24 were created by Dr. McLeod. Part specifications and one figure were obtained from the ThorLabs website. Other part specifications were obtained from Newport Optics and Edmund Optics as relevant.

Chapter 1

Introduction

One of the most exciting projects in modern astronomy is the development and construction of the Giant Magellan Telescope (GMT). With the largest primary mirror surface ever created, the GMT will provide new access to parts of the cosmos that are currently beyond the limits of our observational capabilities. To accomplish this, the GMT relies on sophisticated adaptive and active optics systems that account for both short- and long-timescale variations in mirror shape and position. This system works by using wavefront sensors, which detect aberrations in the shape of the wavefront, to provide useful information to the optical systems that correct for these aberrations. These wavefront sensors are part of the Acquisition Guiding and Wavefront Sensing System (AGWS) probes that are under development at the Smithsonian Astrophysical Observatory. These probes will monitor the wavefront shape to maintain image quality. Computer simulations have been performed to predict the wavefront control systems' performance, but laboratory tests are required to reduce the uncertainty of their performance. To ensure that we will have sufficient control to observe at the

diffraction limit of the GMT, a telescope simulator called the Wide-Field Phasing Testbed is under development, to allow for a laboratory demonstration of GMT phasing and wavefront control. The lab work encompassed by this thesis is the design of the simplified piston-tip-tilt mirror array, the testing and alignment of this array with the Dispersed Fringe Sensor (DFS) and Shack-Hartmann Wavefront Sensor (SHWFS), design of a simplified off-axis parabolic mirror (OAP) alignment setup, and tests of precision alignment of that setup using a laser tracker and interferometer. To accomplish this, we use DFS and SHWFS analysis software partially developed as a part of Frostig (2018) and modified for the purposes of this work. The development and testing of the Wide-Field Phasing Testbed is an ongoing project that is a collaborative effort of a large group of individuals. This thesis aims to test individual aspects of the future full WFPT and establish methods that will be used in the full telescope simulator.

1.1 The Giant Magellan Telescope

The Giant Magellan Telescope (GMT) is an upcoming Extremely Large Telescope being constructed at the Las Campanas Observatory in Chile. It will offer the largest collecting area ($368m^2$, Fanson et al. (2020)) of any telescope to date, and resolution at least 10 times greater than the Hubble Space Telescope (the current point of comparison for high-quality optical and infrared observations). An artists' rendition of the GMT in its housing is shown in Figure 1.1.

1.1.1 Science Goals

The GMT will offer unprecedented access to knowledge across astronomical subfields. Within the realm of exoplanet hunting, the GMT will offer new observations of planetary systems, likely revealing exoplanets as small as Mars around an M star (Science Advisory Committee & Project Office 2018). The GMT will have the ability to determine small planet masses using very sensitive spectroscopy to measure radial velocity over a short amount of time due to its large collecting area. The high performance adaptive optics in the GMT will enable us to observe the light reflected off of the surface of a planet if observing at the diffraction-limited resolution of the GMT. G-CLEF, the high resolution spectrograph that will be the first instrument used with the GMT, has sufficient spectral resolution to measure the abundances of certain elements (notably, oxygen) in exoplanet atmospheres (Science Advisory Committee & Project Office 2018). The GMT will also be used to study planet formation, both by investigating the chemical species near a star, and by spatially resolving the dust in the circumstellar disk.

The GMT will also inform our understanding of star formation and the lives of young stars. Radial velocity measurements will be used to track the kinematics of young stars in clusters. The GMT Near-Infrared spectrograph will enable direct high-resolution spectral observations of many protostars, which are currently not well understood (Science Advisory Committee & Project Office 2018). The GMT will also enable more accurate stellar mass measurements, including the mass of some stars that are not measurable with our current instruments. With the GMT, astronomers can also endeavor to observe the rare, metal-poor stars that are known to be consequential for current theories of the formation of the first stars.

The GMT will also be used to measure the spectra of distant galaxies, allowing us to

study star formation and galaxy kinematics, as well as the circumgalactic medium. The GMT's unparalleled size and cutting-edge instruments will also likely revolutionize our understanding of dark matter.

A variety of instruments will be used to accomplish the GMT's ambitious science goals. These include spectrographs specially designed to study Earth-mass exoplanets (G-CLEF, Mueller et al. 2018) or distant and nearby galaxies (GMACS, Pak et al. 2020). Because the GMT is a ground-based telescope, it has the advantage that new instruments can (and will) be added to it throughout its lifetime. Observations from the GMT will be combined with observations at other wavelengths (e.g. ALMA, JWST) to investigate many of these topics (Science Advisory Committee & Project Office 2018).

1.1.2 Technical Information

The primary mirror of the GMT has a segmented shape, consisting of one central circular mirror surrounded by 6 identical circular mirrors. Each segment is 8.4 meters in diameter, forming a aplanatic Gregorian optical surface with a total primary diameter of 24.5 meters (Fanson et al. 2020). The mirrors are the largest ever created, and are currently being fabricated at the Richard F. Caris Mirror Laboratory at the University of Arizona. The GMT secondary is also a segmented mirror; at first light, an assembly with fast-steering rigid segments will be used, but it will be replaced with adaptive secondary mirror segments once they are completed. The adaptive secondary will allow for precise control of the mirror figure and enable advanced adaptive and active optical systems. Before the adaptive secondary mirror segments are delivered, the GMT will take images by using active optical control of the primary mirror and controlling the tip

and tilt of the fast-steering secondary mirrors (Science Advisory Committee & Project Office 2018). The challenge of maintaining image quality from segmented mirrors requires excellent wavefront sensing capabilities. Even a misalignment of a few hundred nanometers would compromise image quality. To accomplish this, a suite of instruments will monitor the phasing and alignment of the segments at subapertures shown in Figure 1.2. The development of these sensors is the domain of the the Acquisition, Guiding, and Wavefront Sensing Systems (AGWS) group at Smithsonian Astrophysical Observatory, described in more detail in Section 1.2.

Adaptive Optics

The GMT will utilize sophisticated active and adaptive optics systems to maintain wavefront quality. Active optics (AcO) describes systems that correct for long timescale variations in mirror figure, from causes like temperature gradients and gravitational sag. Adaptive optics, or AO, refers to a system where feedback from the telescope is used to adjust a deformable mirror to account for atmospheric turbulence and other short-time-scale variations (Babcock 1953). The GMT can observe in different adaptive optics modes. These include 'natural seeing', ground layer AO (GLAO), natural guide star AO (NGSAO), and laser tomography AO (LTAO) (Kansky et al. 2020). Natural seeing can be used over the entire wavelength range and field of view of the GMT, and can be accomplished with either the rigid or adaptive secondary (Science Advisory Committee & Project Office 2018). GLAO provides corrections for atmospheric turbulence over a wide field of view, and will be functional with any instruments once the adaptive secondary mirror segments are installed. NGSAO uses a natural guide star

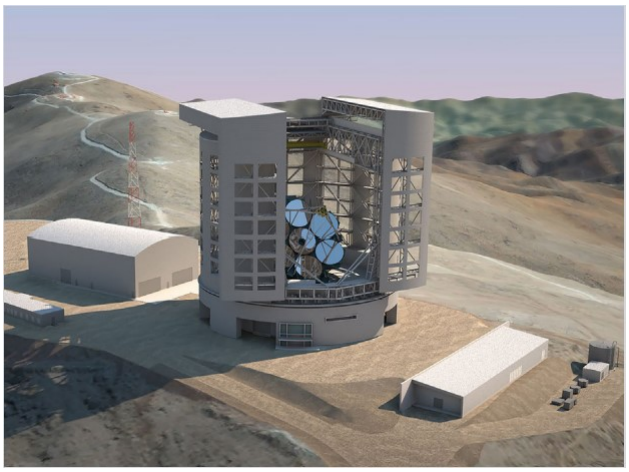

Figure 1.1: The Giant Magellan Telescope in its protective housing, artists' rendition. Figure reproduced from Science Advisory Committee & Project Office (2018), all image credits to GMTO.

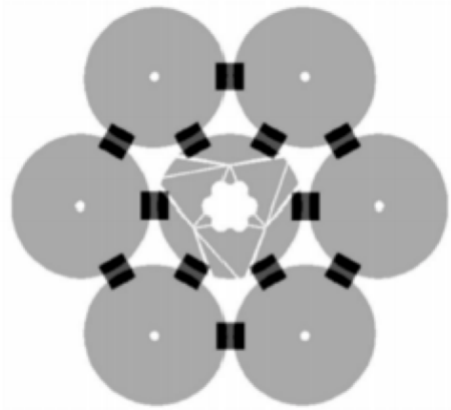

Figure 1.2: GMT pupil shape, with 12 1.5m^2 subapertures placed at segment boundaries. Each gray circle represents a mirror segment 8.4m in diameter.

to provide high quality (as defined by Strehl ratio $> 75\%$) diffraction-limited images over a small field of view at wavelengths $> 0.6\mu m$, and again requires the adaptive secondary mirrors (Science Advisory Committee & Project Office 2018). LTAO uses laser guide stars to produce diffraction-limited medium quality (Strehl ratio $> 30\%$) images of a small field of view at infrared wavelengths, and requires the adaptive secondary mirrors. By having multiple AO modes, the GMT maximizes its ability to take high resolution images of a wide variety of targets, with different ways to optimize depending on the field of view and wavelengths required.

1.2 AGWS

To achieve optimal image quality with the GMT, it is necessary to have precise control over the phasing and alignment of the primary and secondary mirrors. This is accomplished using pneumatic actuators on each primary mirror segment. However, to control these actuators, as well as to correctly position both the primary and secondary mirror segments, it is necessary to obtain information about the wavefront error. When the adaptive secondary mirror is in use, this information also informs the shape of the secondary. This is accomplished using two detectors (see Section 2.3) that measure the phasing and alignment of the mirror segments, which are part of the larger Acquisition Guiding and Wavefront Sensing System.

The Acquisition Guiding and Wavefront Sensing System (AGWS) is a crucial part of the GMT design. AGWS makes the measurements that maintain the alignment, phasing, pointing, and shape of the seven segments of the GMT mirrors. The exact role

of the AGWS varies slightly depending on which AO mode is used. In natural seeing and GLAO, the AGWS is the primary wavefront sensing system for the telescope. In NGSAO, it is responsible for initial phasing of the segments. In LTAO, it maintains the phasing over the course of the observations (Kansky et al. 2020). Regardless of AO mode, the AGWS controls the telescope's active optics (AcO) corrections, which accommodate changes in the segments' geometry and alignment over longer timescales than those corrected by AO. These corrections are especially essential before the adaptive secondary mirror is installed, to provide the information required to control the primary mirror figure and the fast-steering secondary mirrors. Four identical AGWS probes will be mounted to the Gregorian Instrument Rotator at a position 0.5m above the Gregorian focal plane of the GMT. One AGWS probe is shown in Figure 1.3. The probes generally monitor the field of view between 6 and 10 arcminutes off axis, but can be used for GLAO observations of on-axis targets if a mirror is removed (Kansky et al. 2020).

1.3 The Wide-Field Phasing Testbed

In designing in the wavefront control system, the GMT team has largely relied on numerical simulations which include the effects of fabrication errors, atmospheric turbulence, and telescope motion and structural response. Although these are the largest contributors to image quality, laboratory testing of the instruments and control systems will reduce the risk of failure. To ensure that the GMT mirror segments are phased correctly in the diffraction-limited observing modes, the WFPT serves as a telescope simulator for a laboratory demonstration of GMT phasing and wavefront control. It will produce an output beam with the same focal ratio ($f/8.16$), and with the same

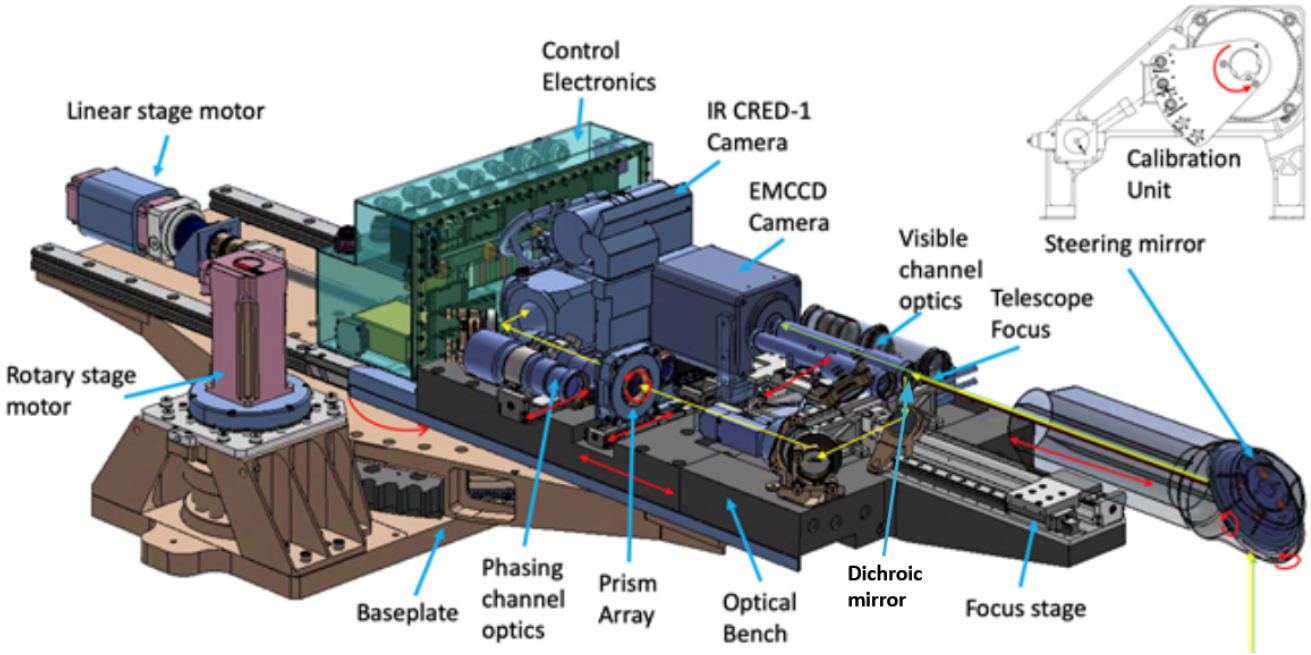

Figure 1.3: AGWS Probe. Visible channel shown in green, infrared channel (for phasing) shown in yellow, and axes of motion showed in red. Figure reproduced from Kansky et al. (2020)

field-dependent aberrations that are expected of the true GMT. This allows us to test the wavefront sensing techniques that will be used on the final GMT.

The goal of this testbed is to serve as a telescope simulator to analyze the behavior of the GMT wavefront control systems, testing both the visible (Shack-Hartmann Wavefront Sensor, see Section 2.3.1) and infrared (Dispersed Fringe Sensor, see Section 2.3.2) channels that will be used on the final AGWS probes. The WFPT will allow for testing of the natural seeing mode, through control of a doubly segmented telescope, as well as testing of phasing and active optics control using off-axis measurements in NGSAO and LTAO. The relation between the GMT, WFPT, and AGWS is diagrammed in Figure 1.4.

1.3.1 Optical Design

To ensure that the WFPT is a sufficiently accurate telescope simulator, there is a set of constraints which it must meet. The WFPT aims to reproduce the wavefront errors caused by the figure errors (deviations from the optics' designed shape) and rigid body motion of each segment. It must output a steerable f/8.16 beam with the GMT pupil shape (as seen in Figure 1.2), which is then measured using the instruments that will ultimately be part of the AGWS probes.

To accomplish this, the AGWS team has designed a series of four optical relays. The first is an entrance relay constructed from off-axis parabolic mirrors (OAPs; see Section 3.1.1) with sufficient space to insert Lexitek phase screens to simulate the effect of atmospheric turbulence. The second is an OAP-based relay that includes a pair of segmented piston-tip-tilt mirror arrays (PTT; see Section 2.2) at an incidence angle of

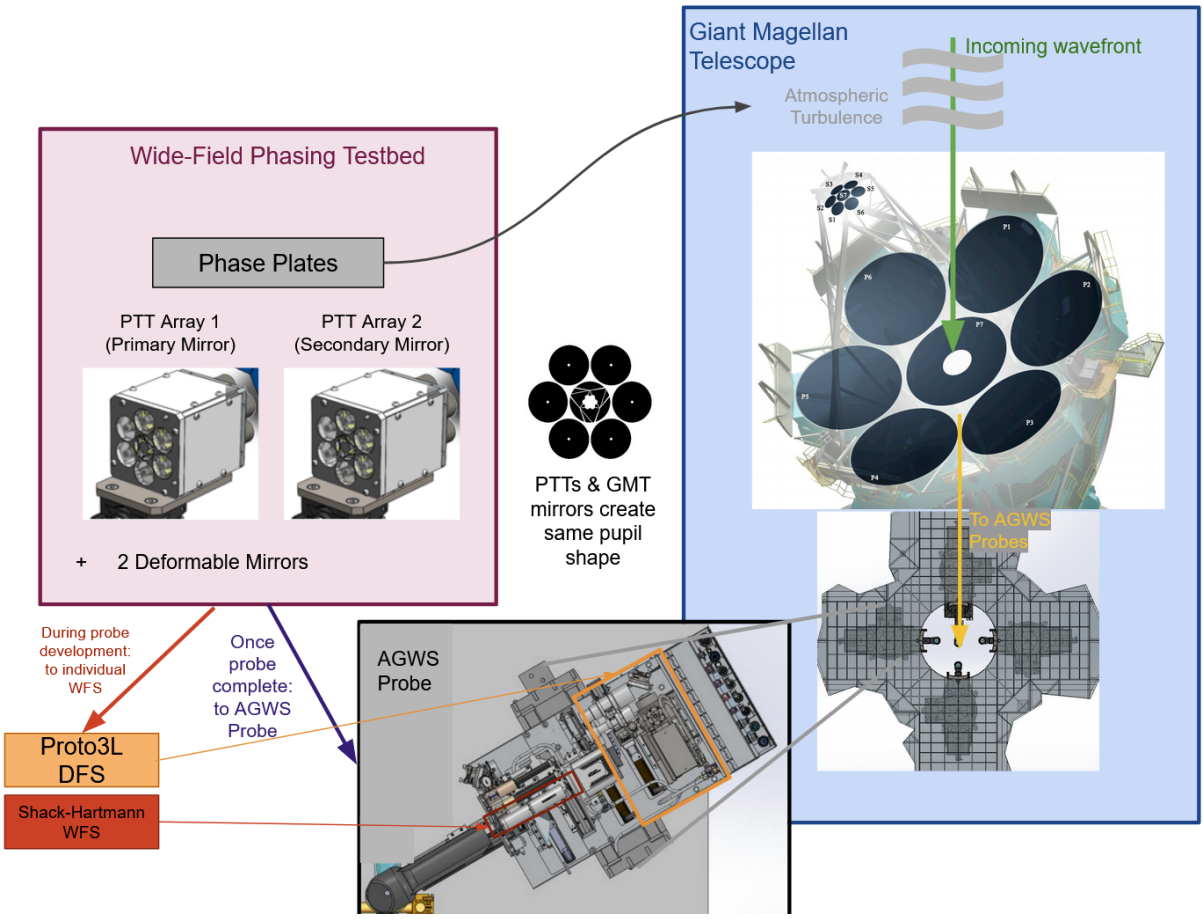

Figure 1.4: Relations between elements of WFPT, GMT, AGWS probes.

8°. The third relay consists of OAPs used to image two deformable mirrors, and the final relay consists of spherical mirrors used to create the necessary focal distance. This is shown in Figure 1.5. The testbed will be analyzed with the first AGWS probe prototype when it is complete, but will first be analyzed with the laboratory prototype dispersed fringe sensor, Proto3L, and a separate SHWFS.

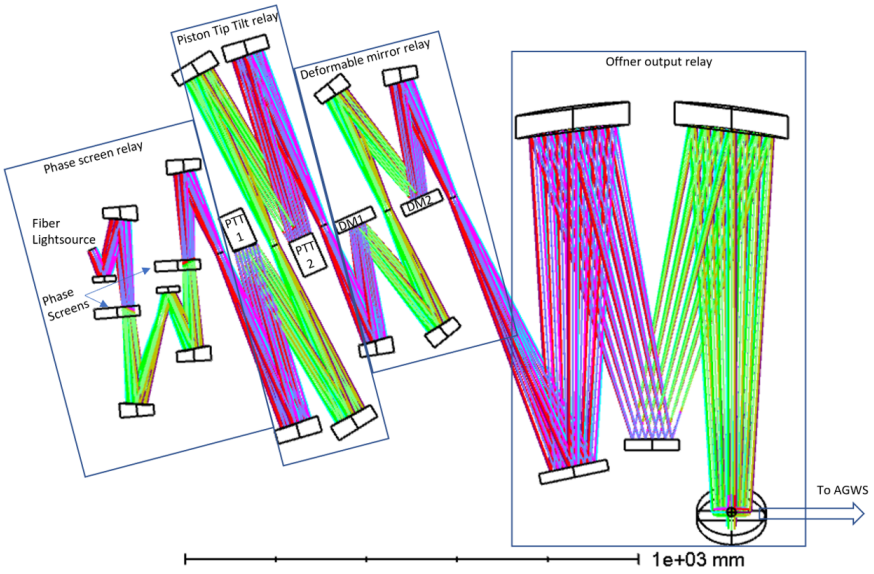

Figure 1.5: Reflective testbed optical design, featuring a very compact configuration of the main relay optics. Reproduced from McLeod et al. (2021)

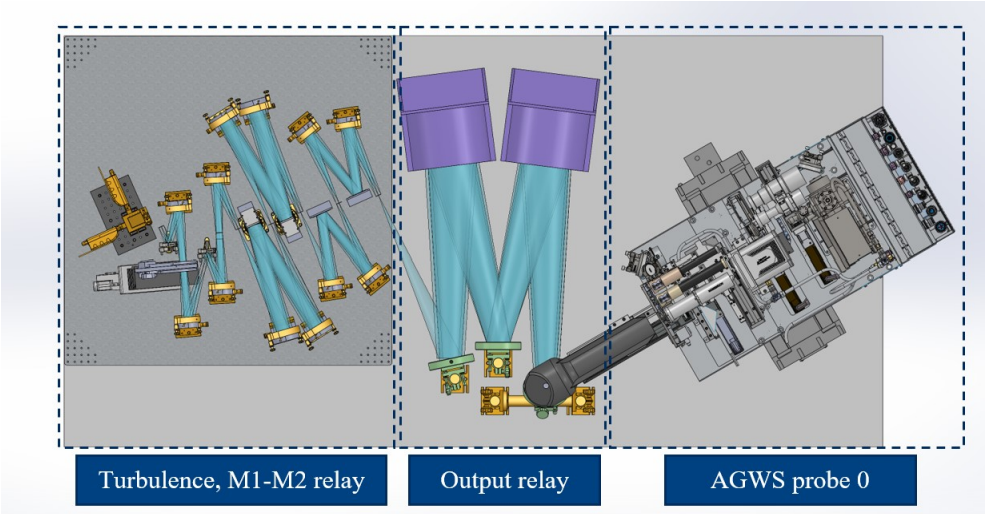

Figure 1.6: Reflective testbed mechanical design, as modeled in SolidWorks. Reproduced from McLeod et al. (2021)

1.3.2 Preliminary Testing

Before the assembly of the complete WFPT shown in Figures 1.5 and 1.6, it is necessary to test individual aspects of the WFPT. This includes the construction of prototypes of some complex parts (e.g. the piezo-actuated piston-tip-tilt mirror array, see Section 2.2) and the testing of planned methodologies (e.g. aligning off-axis parabolic mirrors, see Section 3.3.2). Most importantly for the scope of this thesis, it also requires determining the accuracy and precision of the sensors and measurement devices. If the planned setup is not sufficiently sensitive, it will not serve as an effective telescope simulator to understand the performance of AGWS devices. Therefore this thesis aims to establish constraints on the measurement capabilities of the Shack-Hartmann wavefront sensor, Dispersed Fringe Sensor, and laser tracker.

1.4 Outline

The format of this thesis is as follows. Chapter 2 describes wavefront sensing systems and their testing, including the Shack-Hartmann wavefront sensor and the Dispersed Fringe Sensor. Chapter 3 describes steps taken toward aligning a pair of off-axis parabolic mirrors, using a laser tracker and an interferometer. Chapter 4 summarizes the findings of this thesis and future related work. The appendix contains a list of abbreviations, as well as a sampling of Dispersed Fringe Sensor and Laser Tracker data.

The research described in this thesis was performed as a part of the larger efforts of the whole GMT and AGWS team. This thesis primarily aims to summarize and report the work and findings of the author of this thesis. The design, wiring, and assembly of, for

example, the Proto3 Dispersed Fringe Sensor or the piezo-actuated piston-tip-tilt mirror array, are collaborative products of the team and are beyond the scope of this thesis.

Chapter 2

Wavefront Sensing

2.1 Background

Wavefront sensing is the study of the aberrations and shape of a wavefront. In the context of the GMT, this is especially important because of the segmented geometry of both the primary and secondary mirrors. Maintaining image quality requires accurate phasing of the mirror segments, and wavefront sensors enable us to understand when the system is not aligned correctly, and therefore to use AO or AcO to fix it. The sensors described in this section aim to precisely measure the wavefront error across the boundaries between mirror segments. This is accomplished in a laboratory setting by constructing mirror arrays that have boundaries between segments, and that have the same degrees of freedom (piston displacement, tip, and tilt) as the real GMT mirrors. For preliminary testing of the sensors, we first begin with a simplified testbed design, diagrammed in Figure 2.1 and shown in Figure 2.2. This consists of a pinhole light source, a collimating lens (focal length 143.8mm), a simplified prototype of the piston-tip-tilt

mirror array, a focusing lens (focal length 200mm), and a dichroic mirror to transmit IR wavelengths and reflect visible wavelengths. The visible light is passed into the Shack-Hartmann wavefront sensor, which measures tip and tilt error, and the infrared light is passed into the dispersed fringe sensor, which measures piston error. These devices are described in more detail in Section 2.3.

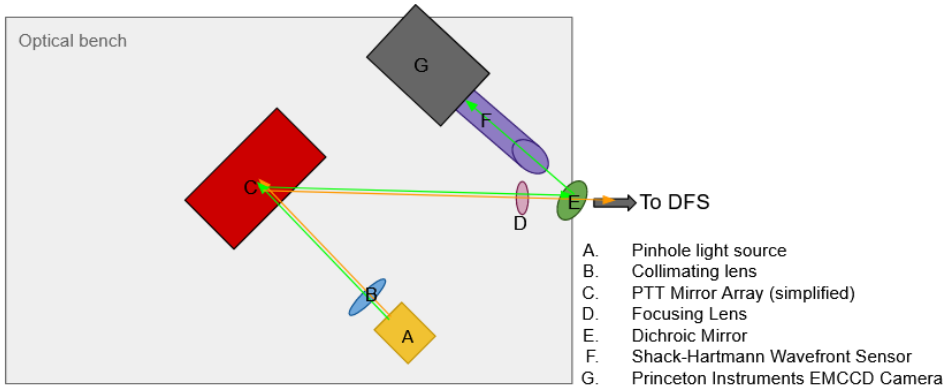

Figure 2.1: The optical bench setup for preliminary testing. The orange arrow represents the infrared path and the green arrow represents the visible path. More detail on the sensors mentioned here is available in Section 2.3.

The wavefront sensing tests occur on an optical bench in a laboratory tent at the Smithsonian Astrophysical Observatory Cambridge Discovery Park location. This tent is enclosed in TRAX Industrial Black Curtains, which were determined in Frostig (2018) to be sufficient to block stray IR light from elsewhere in the laboratory.

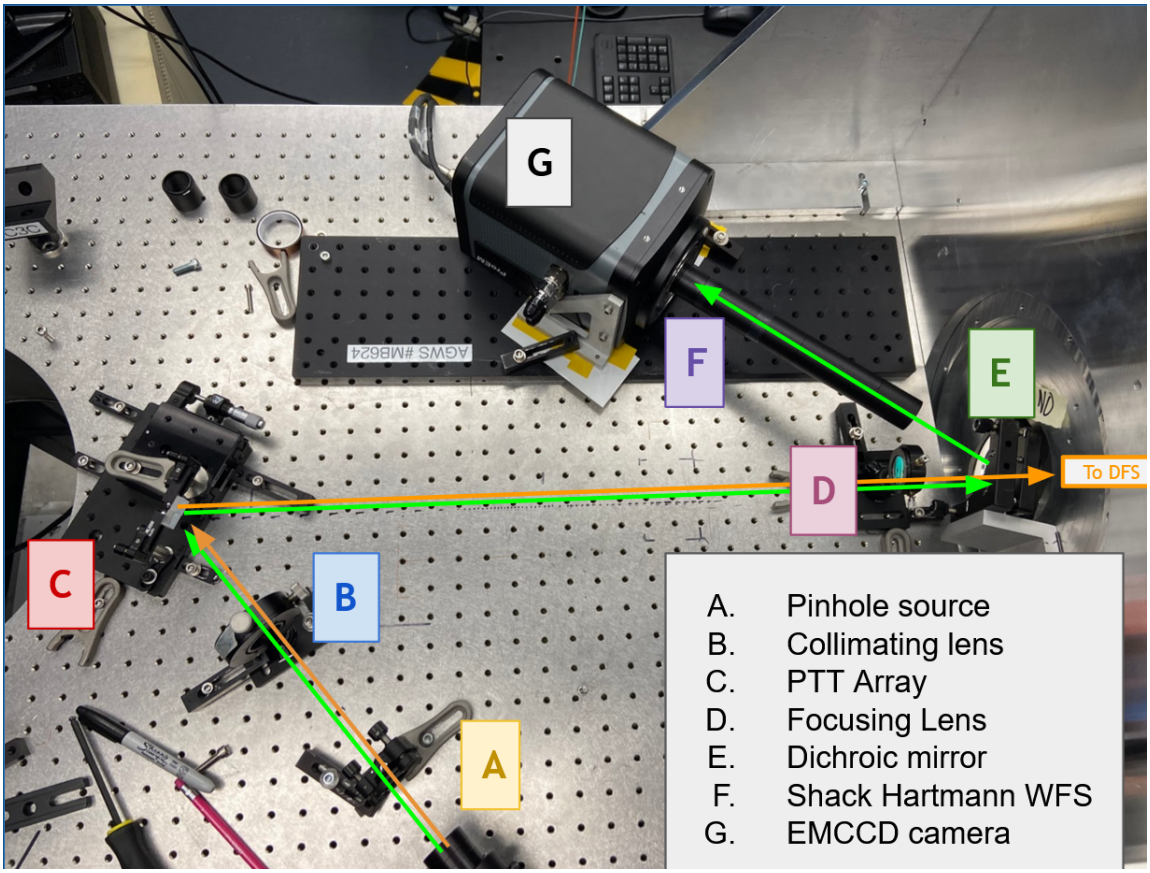

Figure 2.2: The optical bench setup for preliminary testing.

2.2 Piston-Tip-Tilt Mirror Array Prototypes

To ensure correct phasing of the GMT mirror segments, we must analyze the wavefront behavior at mirror boundaries. This will be accomplished in the final WFPT using mirror arrays that replicate the GMT primary mirror geometry. The piston-tip-tilt (PTT) mirror array is designed to have the same degrees of freedom that the true GMT primary mirror will. In the full WFPT this will be accomplished with a piezo-actuated seven-segment array. (Piezoelectric actuators are electronic devices that change length in response to an applied voltage.) A two-facet piezo-actuated prototype is under construction and will be used for testing. A manual two-facet prototype was designed

and constructed by the author of this thesis and analyzed with both the Dispersed Fringe Sensor and the Shack-Hartmann wavefront sensor.

2.2.1 Main Seven-facet Prototype

Seven hexagonal mirrors (each 17mm across) will be arranged to cover a pupil 50.25mm in size. Figure 2.3 shows the CAD model of the PTT array prototype. Two identical PTT arrays will be used, each with a mask defining the clear aperture and other nearby physical obstacles, so as to generate the same vignetting as a function of field position that will be observed at the GMT. The main PTT array mirrors will be mounted on a Thorlabs GNL18-M stage for pitch adjustment and a Newport RSP-2T stage for yaw adjustment as shown in Figure 2.4. For piston displacement and tilt adjustment, the mirrors are each affixed to 3 Thorlabs PK4FYC2 piezo actuators at the locations shown in Figure 2.5. These piezos have a total functional distance of 38μm. In the design of the PTT array, 7.1μm has been allotted as the assembly tolerance, which will create an angular displacement of 0.88 mrad, which we intend to measure with the Shack-Hartmann wavefront sensor described in the next section. After the mirror array's initial assembly, the DFS and SHWFS will be used to precisely flatten the array by aligning the mirrors. This provides a benchmark which we must ensure our wavefront sensors are sufficiently sensitive to detect.

2.2.2 Two-facet Piezo-actuated Prototype

A two-facet prototype has been constructed following the same specifications that will be used in the final seven-facet prototype that fully replicates the GMT pupil shape. A

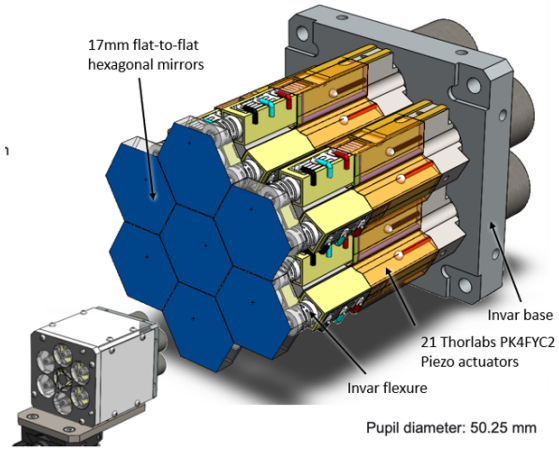

Figure 2.3: The front view of the piston-tip-tilt mirror array. Mirrors are shown in blue. Figure reproduced from McLeod et al. (2021).

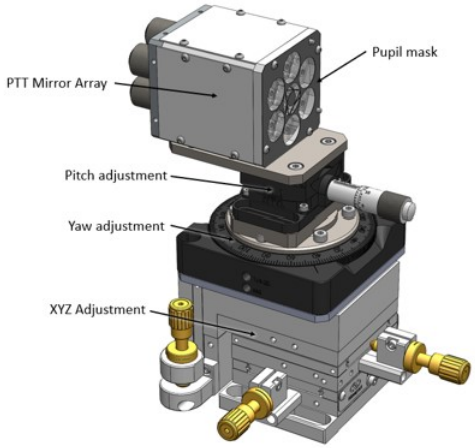

Figure 2.4: Mounted piston-tip-tilt mirror array. Figure reproduced from McLeod et al. (2021).

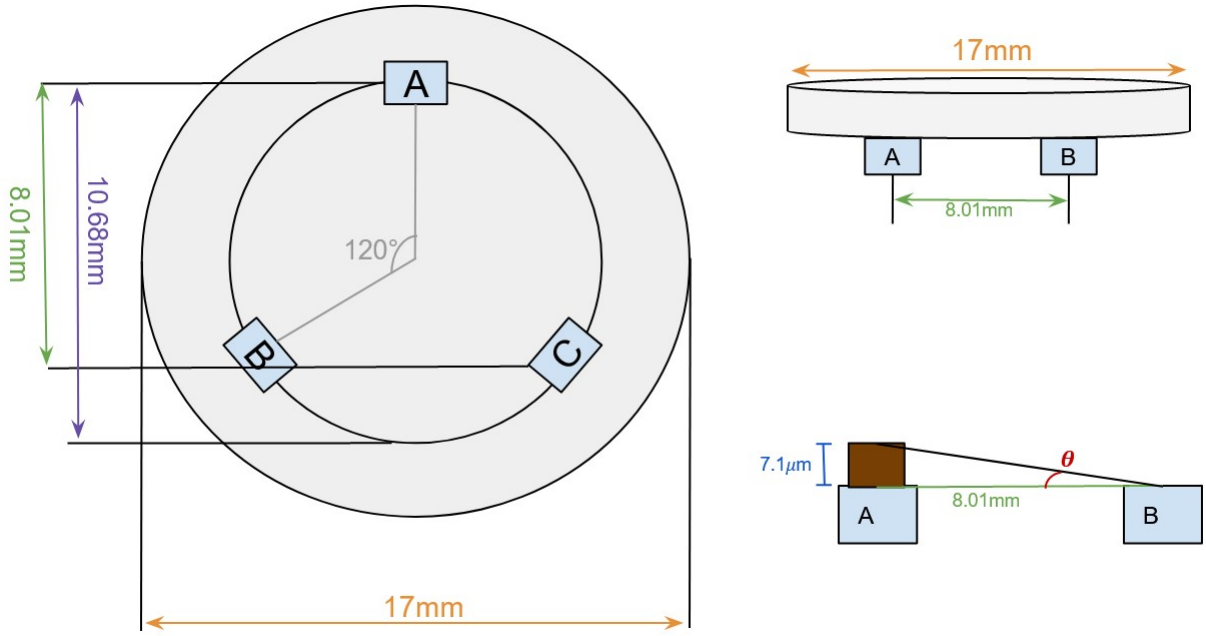

Figure 2.5: A single mirror facet from the PTT array, shown with actuator locations labeled A, B, and C. *Lower right:* The angle, θ, created by an actuator difference of 7.1μm, the assembly tolerance allotted for in the design budget.

17mm hexagonal mirror will be affixed to 3 Thorlabs PK4FYC2 piezo actuators to allow for control of segment positioning, and placed next to a fixed 17mm mirror segment. The actuators will be attached at the positions shown in Figure 2.5. Figure 2.6 shows a computer model of the two-segment mirror assembly. Results from this prototype are presented in Section 2.4.

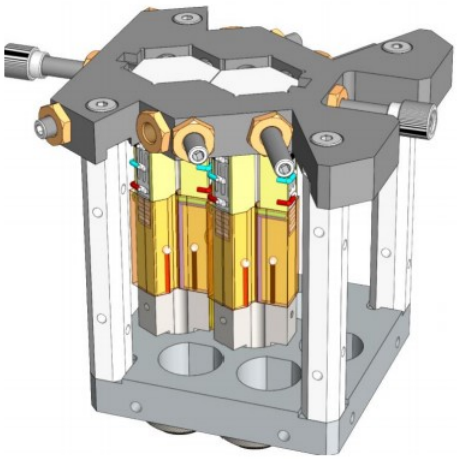

Figure 2.6: Model of piezo-actuated two facet prototype.

Preliminary Two-facet Prototype

While the piezo driven two-element array was being manufactured, we constructed a simplified prototype of a piston-tip-tilt array to measure phasing across the intersection between two mirrors. Two 12.7mm square mirrors (ThorLabs) are secured to metal pieces that are held in kinematic mounts, allowing $\pm 4^\circ$ of rotation in both tip and tilt. One mount is secured to a Newport model 420 translation stage to allow for up to 25.4 mm of piston displacement between the mirrors. This setup is shown as a diagram in Figure 2.8 and as a photo of the laboratory setup in Figure 2.9.

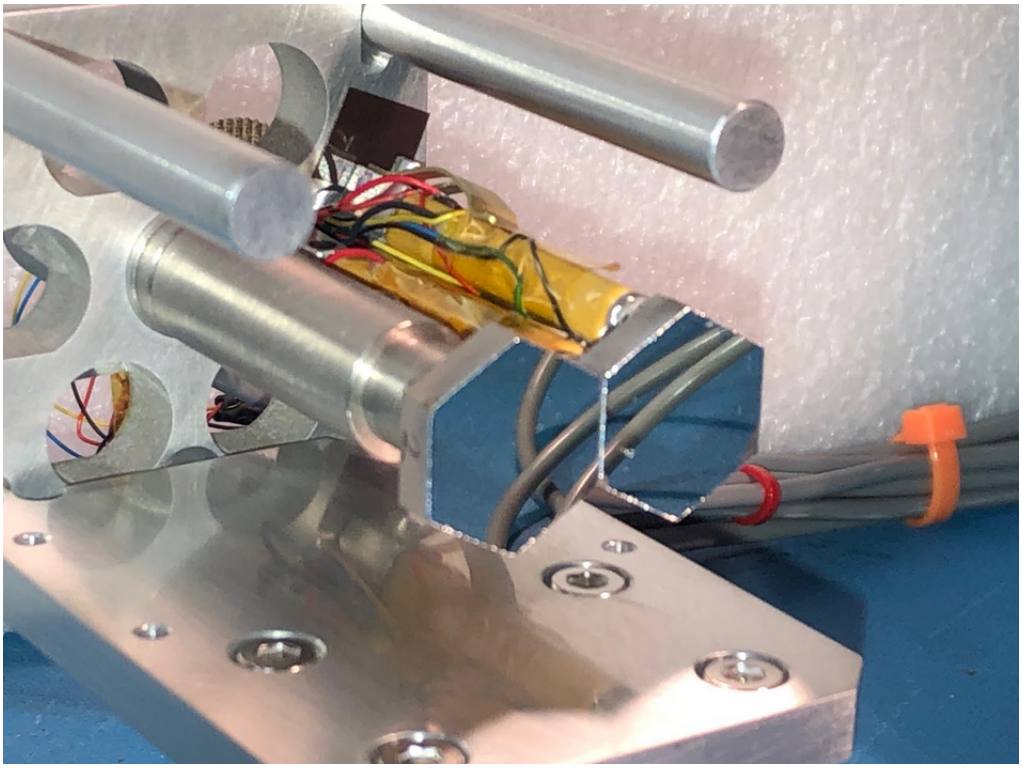

Figure 2.7: Two-facet piezo driven PTT array prototype.

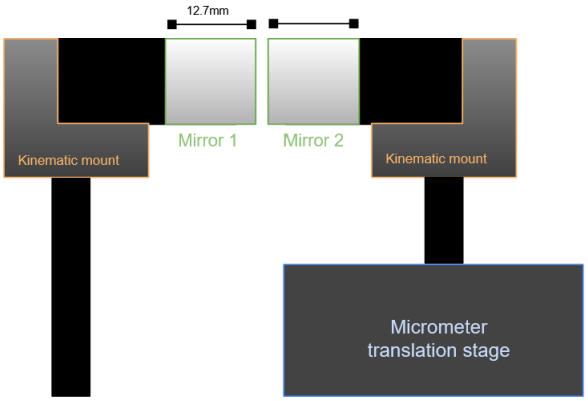

Figure 2.8: Diagram of simplified piston-tip-tilt mirror array used for initial testing. (Separation between mirror facets not to scale.)

2.3 Sensors

2.3.1 Shack-Hartmann Wavefront Sensor

A Shack-Hartmann wavefront sensor (SHWFS) is an optical device used to measure wavefront errors. The history of the SHWFS is summarized in Platt & Shack (2001). The "Hartmann Screen" test had been invented around 1900 to more easily focus telescopes by using two photographic plates (one in front of the focus, and one behind) and placing a large mask with holes in it over the aperture of the telescope (Platt & Shack 2001). The telescope could then be focused by aligning the images from every distinct hole, and the figure of the mirror could also be checked. Roland Shack improved upon this "Hartmann Screen" test by using a lenslet array instead of a mask with holes. This focuses the light into disparate spots and maximizes the sensitivity of the sensor in low-light conditions. These improvements make the SHWFS more practical for astronomical applications.

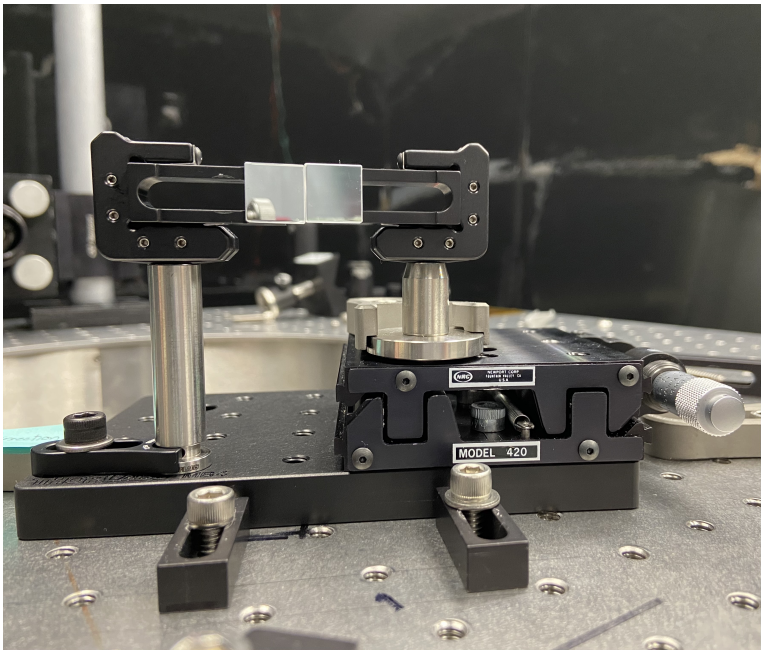

Figure 2.9: Simplified piston-tip-tilt mirror array featuring two 12.7mm square mirrors and kinematic mounts; the right mirror is mounted on a micrometer stage to allow for translation.

Theory

The SHWFS images the aperture onto a lenslet array, which separates the incoming wavefront into different spatial samples, or subaperture spots. The lenses within this array focus the spots onto the detector, where the pattern of spots can be analyzed to reconstruct the shape of the original wavefront. Figure 2.10 shows the behavior of a SHWFS imaging both a plane wave and a distorted wavefront. The fiducial spacing between the spots (i.e. the pattern seen in the plane wave case) is determined by the lenslet array geometry.

SHWFS are widely used in astronomy because they do not require a collimated incident beam and are achromatic, as well as being functional with both low-photon-count and

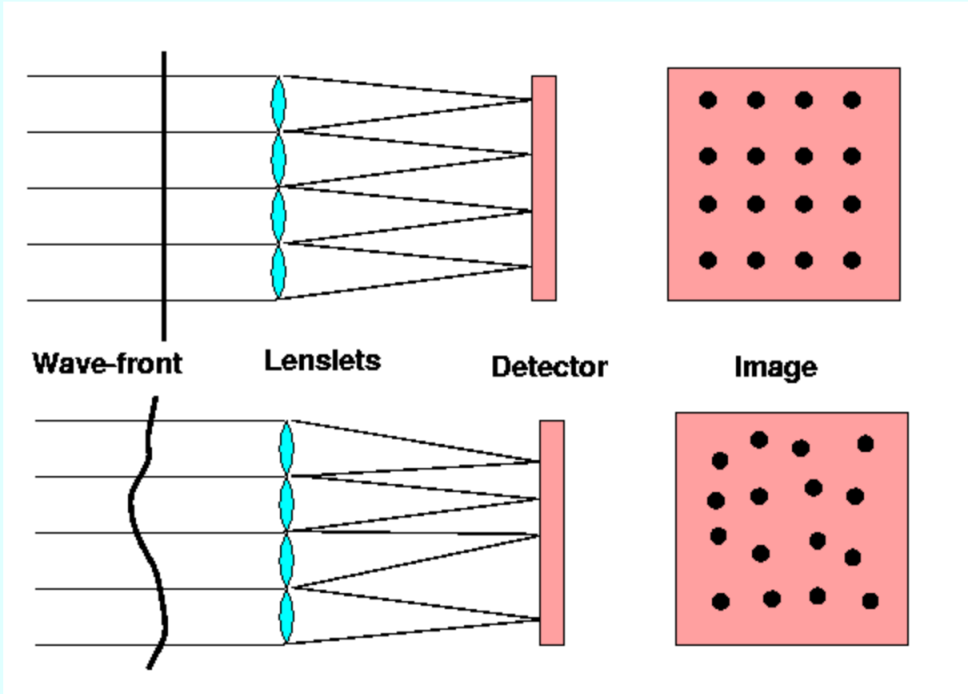

Figure 2.10: *Upper Image:* A Shack-Hartmann Wavefront Sensor imaging a planar wavefront, creating an evenly spaced grid of spots. *Lower Image:* A SHWFS imaging a distorted wavefront, creating an uneven grid of spots. (Figure reproduced from A. Tokovinin NOAO Adaptive Optics tutorial.)

extended sources (Woods 2009). Wavefront sensors are required for both active and adaptive optics systems. A SHWFS can be used to measure the alignment error between the primary and secondary mirrors in an optical system like the GMT, enabling the adjustable mirror support structure to accommodate it appropriately.

The wavefront slope error, T [radians] can be calculated for a specified δx [pixels] using

$$T = \frac{\delta x}{2} \frac{p}{206265} \tag{2.1}$$

where p is the plate scale [arcsec/μm] and the constant factor 206265 serves to convert from arcseconds to radians (Woods 2009). The optimal design of a SHWFS depends on the specific characteristics of the optical system it will be used with, including its focal

ratio and the expected magnitude of the slope errors. Subaperture sampling must be fine enough to reconstruct the wavefront shape from the piecewise linear approximation of its gradient, but not so fine that adjacent spots blend or overlap. The pitch of the lenslet array (often represented with Δ) is chosen to prevent the latter from occurring, as the maximum spot displacement (δ_{max}) depends on the pitch and spot width (W), as shown in Equation 2.2 (Goodman 1996; Woods 2009)

$$\delta_{max} = \frac{1}{2}(\Delta - W) = \frac{1}{2}\left(\Delta - \frac{2\lambda f_{LA}}{\Delta}\right) \tag{2.2}$$

where λ is the wavelength and f_{LA} is the focal length of the SHWFS lenslet array.
To determine the aberrations present in the system, we must analyze the spot pattern created by the subapertures. This is done using the standard Zernike circle polynomials, which are convenient due to their orthogonality over the unit circle and the ease of separating into angular and radial functions. Table 2.1 is a reproduction of Table 5.2 from Woods (2009) and lists the first thirteen Zernike polynomials, with indices j, n, m representing polynomial number, radial degree, and azimuthal frequency. Visual representations of these aberrations are shown in Figures 5.6a-l of Woods (2009). Each Zernike polynomial corresponds to a known wavefront aberration. For example, piston displacement produces a constant phase shift, errors in tip and tilt produces linear phase shifts in x and y respectively, and a defocus error appears as a quadratic phase difference.

Design

Simple procedures for the design and construction of SHWFS are summarized in Woods (2009) and Pernechele et al. (2000). Here, I will describe the SHWFS used in our

j	**n**	**m**	Z_j	**Aberration**
1	0	0	1	piston
2	1	1	$2\rho cos(\theta)$	x-tilt
3	1	1	$2\rho sin(\theta)$	y-tilt
4	0	2	$\sqrt{3}(2\rho^2 - 1)$	defocus
5	2	2	$\sqrt{6}\rho^2 sin(2\theta)$	astigmatism at 45°
6	2	2	$\sqrt{6}\rho^2 cos(2\theta)$	astigmatism at 0°
7	1	3	$\sqrt{8}(3\rho^3 - 2\rho)sin(\theta)$	y-coma
8	1	3	$\sqrt{8}(3\rho^3 - 2\rho)cos(\theta)$	x-coma
9	3	3	$\sqrt{8}\rho^3 sin(3\theta)$	y-trefoil
10	3	3	$\sqrt{8}\rho^3 cos(3\theta)$	x-trefoil
11	0	4	$\sqrt{5}(6\rho^4 - 6\rho^2 + 1)$	spherical
12	2	4	$\sqrt{10}(4\rho^4 - 3\rho^2)cos(2\theta)$	secondary astigmatism at 0°
13	2	4	$\sqrt{10}(4\rho^4 - 3\rho^2)sin(2\theta)$	secondary astigmatism at 45°

Table 2.1:: The first thirteen standard Zernike circle polynomials in spherical coordinates, and the common names for the optical aberrations they produce. ρ represents the radial coordinate and θ represents the azimuthal coordinate. Reproduced from Woods (2009).

experiments. The Shack-Hartmann wavefront sensor used within these experiments is contained entirely within a 1-inch diameter ThorLabs SM-threaded tube, mounted directly to a Princeton Instruments ProEM Series 512B EMCCD Imaging Camera (pixel size $16\mu m$) using a ThorLabs CM1L10 extension tube. The device consists of a 25.4mm-diameter lens (focal length 97.158 mm) and a lenslet array (focal length 26.831 mm, pitch 300 μm), separated by a distance of 127.91mm. The lenslet array

produces spots with a fiducial separation of $300\mu m$, or 18.75 pixels on the EMCCD. A circular aperture with an opening 5mm in diameter is placed in front of the lenslet array to truncate the spatial extent of the dots to prevent confusion due to the spot pattern filling the entire detector. The SHWFS and camera are shown in Figure 2.11. The optical prescription for the Shack-Hartmann optics is shown in Table 2.2. Using equation 2.2, at a wavelength of 1μm, the calculated maximum spot displacement is $\delta_{\max} = 60.56\mu\text{m} = 3.78$ EMCCD pixels.

Based on the optical prescription shown in Table 2.2, we can calculate the spot

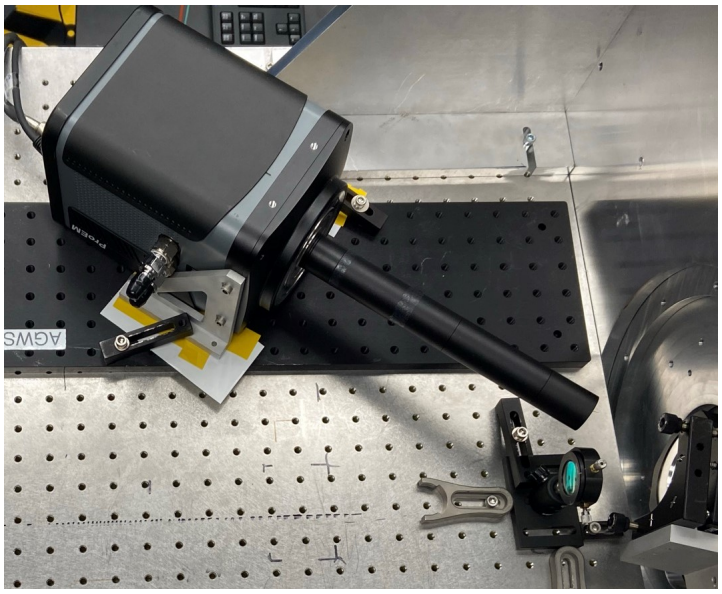

Figure 2.11: Princeton Instruments EMCCD camera and Shack-Hartmann wavefront sensor assembled within a 1" diameter tube.

displacement that will be measured on the detector for a collimated beam entering the first lens ($f = 200$mm, lens D in figure 2.1) at an angle of θ_1. Equations 2.3 and Figure 2.12 show this relation, where d_2 is the displacement that will be measured on the final

Description	Radius	Thickness	Material
Telescope Focus	Infinity	97.158	
ThorLabs AC254-100-B	259.400	1.500	N-SF6HT
	53.700	4.000	N-LAK22
	-66.700	127.910	
Lenslet Array	Infinity	1.000	F_ Silica
	-12.200	26.831	
CCD			

Table 2.2:: The optical prescription for the Shack-Hartmann Wavefront Sensor.

detector.

$$\begin{aligned} d_1 &= f_1 tan(\theta_1) \\ \theta_2 &= arctan\left(\frac{d_1}{f_2}\right) \\ d_2 &= f_3 tan(\theta_2) \end{aligned} \tag{2.3}$$

where the variables have the meanings shown on Figure 2.12; d_2 is the crucial parameter that describes the displacement of a spot on the detector. For our SHWFS, $f_1 = 200$mm, $f_2 = 97.158$mm, and $f_3 = 26.831$mm. One full rotation of the knob in the mounts for the simplified PTT array corresponds to 13.4 mrad of surface rotation, which deflects the wavefront by a total of 26.8 mrad. We can now calculate that a tilt wavefront deflection of 1 mrad corresponds to a relative translation of 3.45 pixels, or 55.2 μm, on the EMCCD detector.

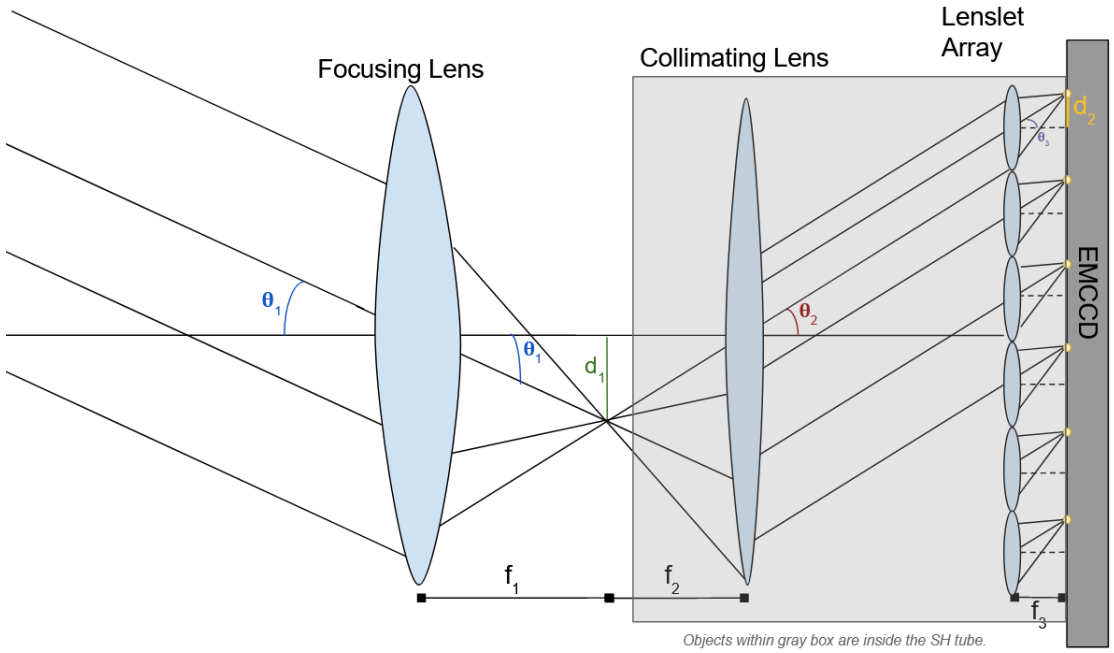

Figure 2.12: Diagram representing the optical path through the focusing lens and the Shack-Hartmann Wavefront Sensor, ending on the EMCCD. Geometric relations defined in Equation 2.3.

Testing and Analysis

The mirror segments (see Section 2.2) are aligned in tip and tilt by adjusting them until the pattern of dots produced by the SHWFS is an even grid with no discontinuities in rows or columns. This is shown in Figure 2.13. To determine the local wavefront slope error, we must calculate the spot displacement of each pixel. This is accomplished using Python to perform a least squares fit to acquire the location of each spot in the image and compare it to an evenly spaced grid and calculate the displacement. The spot displacements can be used to compute the Zernike aberration coefficients and therefore the corresponding aberrations. Once the set of aberrations is known, they can be used to evaluate the image blurring that would be observed on-sky and therefore also as a part

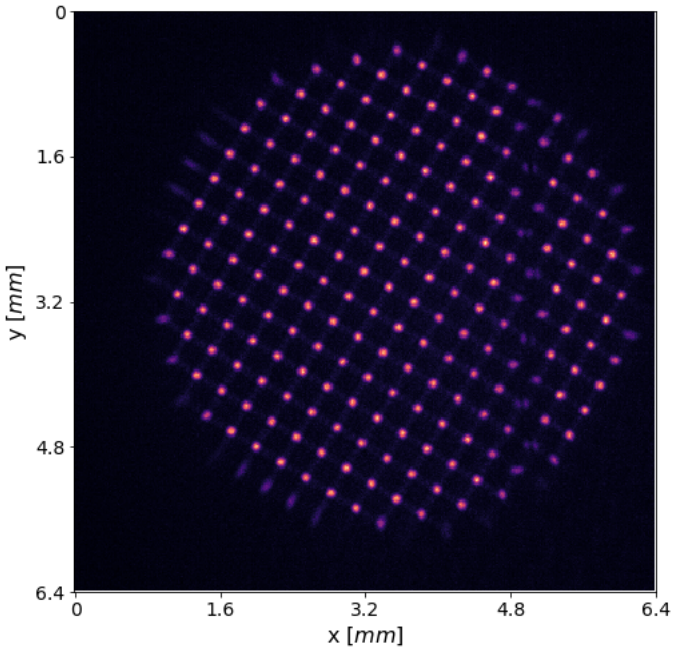

Figure 2.13: Shack-Hartmann Wavefront Sensor image of coplanar mirrors in simplified PTT array. The intersection between mirrors is the vertical line of dimmer spots around $x = 5$mm. Spots to the right of this line represent reflections off one mirror facet; spots to the left represent reflections off the other mirror facet.

of AO/AcO systems.

Our data processing software selects spots that have a flux above the minimum specified flux fraction and are within the defined maximum pupil radius (both user-defined). It computes the centroid of each spot as well as the reference positions of each spot on the evenly-spaced grid. It then calculates each Zernike aberration coefficient and computes the model and residuals. To analyze data from the two-mirror PTT prototype described in Section 2.2, we must be able to identify spots that are reflected off of each facet of the mirror. This is done by requiring the user to specify two points on the line separating the

facets on the SH images. The spots are then identified as either belonging to mirror 1 or mirror 2. This allows two additional terms to be computed that are used to calculate the x-tilt and y-tilt error and therefore provide the key information about the relative tilt between the mirror facets.

Results

To test the Shack-Hartmann Wavefront Sensor, we measure the translation and motion of the spots as described above.

Using the analysis software described in the previous section and data with small incremental adjustments between images, we measure relative tilt differences of $\sim 0.1 - 1$ mrad in most images. These values correspond to translations of $0.3 - 3.5$ pixels, which are smaller than the value of $\delta_{\max} = 3.78$pix calculated using equations 2.2. We can plot the displacement of each spot relative to its reference position with a vector, as shown in Figure 2.14. This is useful to visualize the aberrations. We estimate the precision of the SHWFS by measuring the RMS of the residuals of the Zernike fit. For our observations using the preliminary two-segment manual PTT array, the RMS of the fit residuals is 0.5 pixels for each spot, which corresponds to an error on the mean of $0.5/N_{\text{spots}} \geq 0.1$ pixels. This corresponds to a wavefront deflection of 0.03 mrad. We therefore estimate that the precision of our fit is approximately 0.1 pix = 0.03 mrad.
Measuring the stability of the SHWFS over time is accomplished by taking 20 exposures over a period of 20 minutes, first using the simplified manual PTT (piezo-actuated prototype results are presented in Section 2.4). From this data we find a tilt difference of 0.227 ± 0.082 mrad, indicating that the current setup is not stable over time. However,

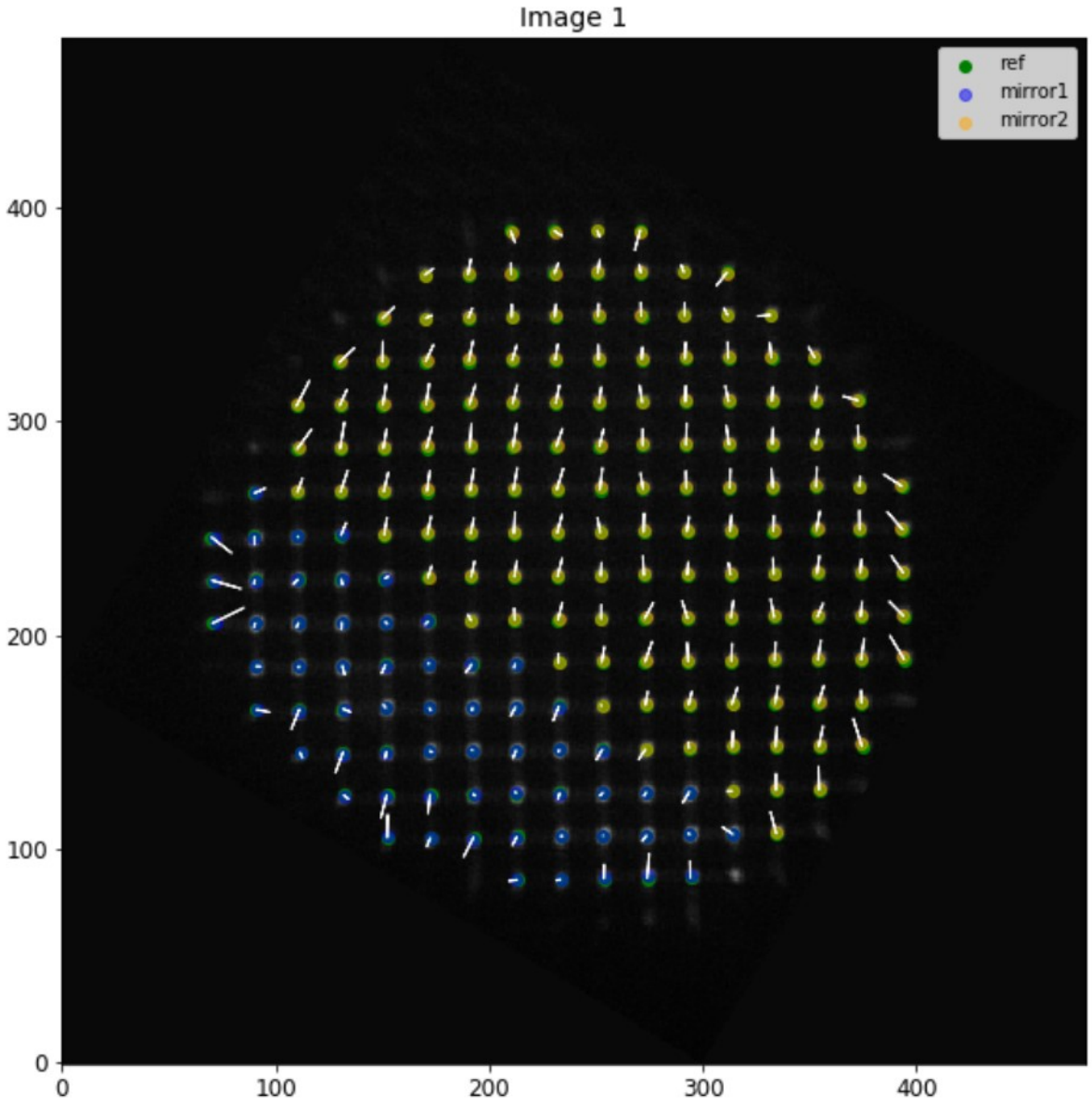

Figure 2.14: SHWFS image, considered coplanar by eye. The SH analysis code described in Section 2.3.1 calculates a difference of 4.11 mrad between the mirror facets. The reference positions of each spot with the fiducial spacing are shown in green, and overlaid with spots colored either blue or orange to differentiate between the mirror facets. The white lines are vectors representing the difference between the reference spot and the measured spot, and are scaled up by a factor of 10 for ease of visibility.

this is of little consequence for the final WFPT assembly using the piezo-actuated PTT arrays. We can therefore also estimate the precision from the standard deviation of the stability data measurements; this yields a value of 0.082 mrad, corresponding to a shift on the EMCCD detector of 0.284 pixels. Comparing the two measures of precision, we determine the precision of our measurements to be 0.082mrad, taking the more conservative value.

Additionally, we have determined that we can use the SHWFS described herein to flatten the main seven-segment PTT array described in 2.2, because as shown in Figure 2.5, the angle created by the assembly tolerance of 7.1μm is $\theta = 0.88$ mrad, which is much greater than our SHWFS' sensitivity of 0.082mrad. This angle corresponds to a translation on the detector of ~ 3 pixels, or 48.6μm.

The SHWFS software analysis code is able to analyze a single image (exposure time 1100 ms) in 90ms, and a batch of 20 images in 1.74 seconds. It is sufficiently fast to allow for real-time analysis of data as they are obtained.

2.3.2 Dispersed Fringe Sensor

To obtain images at the diffraction-limited resolution of the GMT, it is necessary to maintain not just the relative tip and tilt of the GMT mirrors, but also their piston phase difference. The SHWFS described in the previous section is not sensitive to motion along the optical axis, so another optical device is necessary. For this purpose, a dispersed fringe sensor (DFS) will be used.

Theory

The DFS on the GMT uses light from the boundaries between segments to analyze the phasing of the segments (see Figure 1.2). Each subaperture spans an area of 1.5 m^2, large enough to capture sufficient light but small enough to maintain phasing within a subaperture. Each of these subapertures creates a diffraction pattern for each wavelength, which is then dispersed perpendicularly using a prism array, creating a fringe pattern. The spacing of this fringe pattern is linearly dependent on wavelength. Fringes at different wavelengths shift by a different amount for the same piston phase difference, causing the fringes to tilt. Therefore, we know that if the fringes appear tilted, there is a phase difference between the mirrors. By Fourier transforming the fringe image, we can estimate a measurement of the piston phase difference error by comparing the peak of the central lobe and the peak of the side lobes. This is shown visually in Figure 2.15.

Design

The current DFS prototype (Proto3L) is shown in Figure 2.16. Light enters from the optical bench (or the telescope) and is reflected upward and through either a mask (shown in left subfigure of Figure 2.16) or a lens, and then through either a prism array (for fringe viewing) or a lens (for pupil or unobscured viewing). The image is then reflected onto the camera. The DFS is designed to be used in the near infrared, at J-band wavelengths ($\approx 1.2\mu$m), which were determined in simulations to optimize the sensitivity and minimize the effects of atmospheric turbulence and thermal noise (van Dam et al. 2016).

Images can be taken with either the Ninox VIS-SWIR 640 (Raptor Photonics)

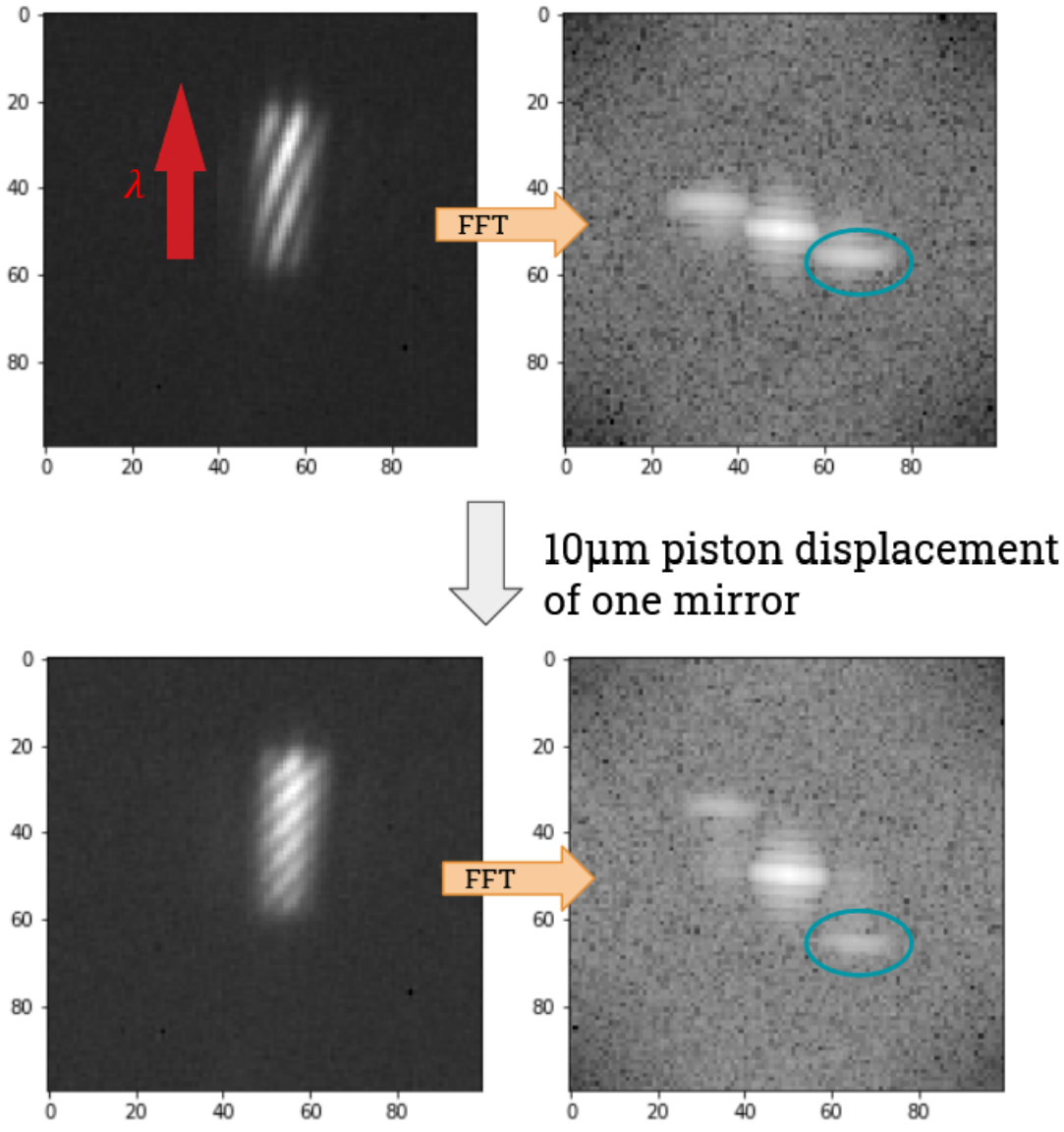

Figure 2.15: Fringes (left) from one subaperture and their fast Fourier transforms (right), both before and after a $10\mu m$ translation of one mirror.

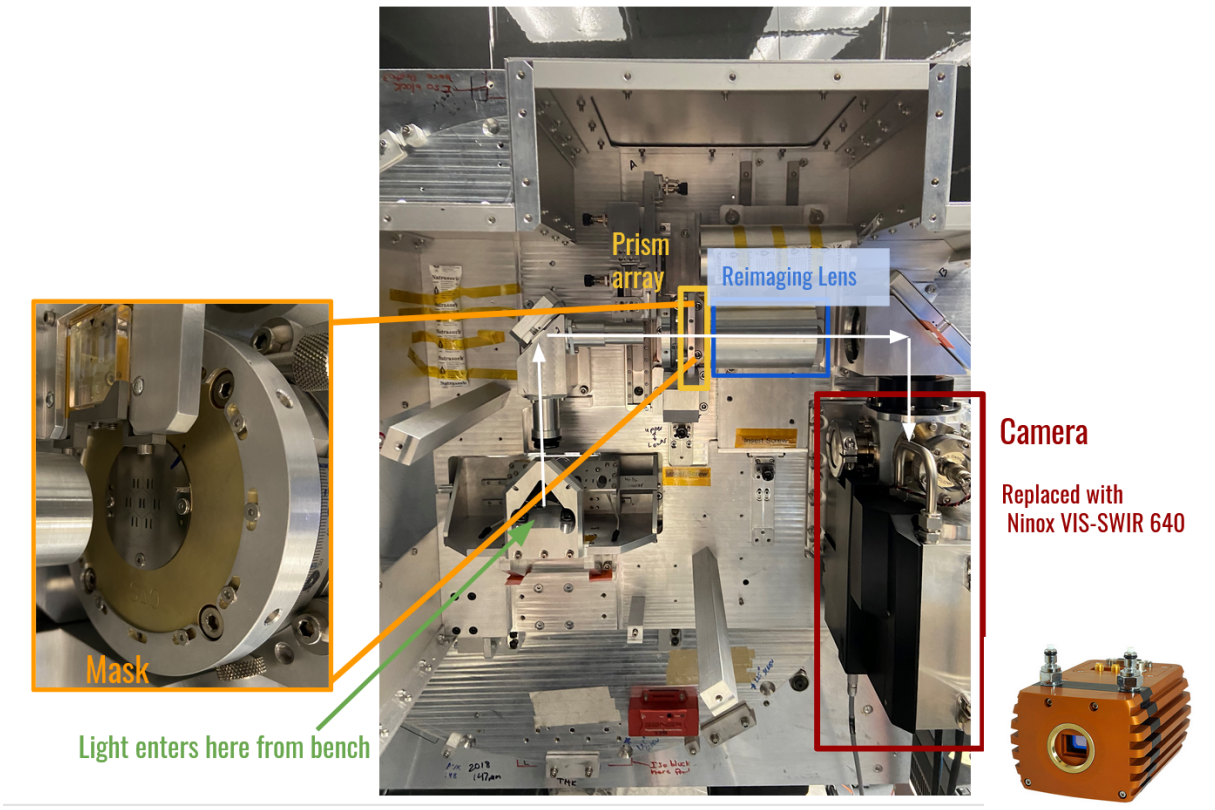

Figure 2.16: The Proto3L Dispersed Fringe Sensor Prototype, shown with the C-RED One camera attached. Optical path represented by white arrows. The mask used to create subapertures as a part of the DFS is shown in subfigure at left.

or the C-RED ONE (First Light Imaging) cameras. The Ninox detector is a 640x512 InGaAs PIN-Photodiode with a pixel size of $16\mu m$, which corresponds to 0.05 arcseconds per pixel. The C-RED ONE uses an electron-initiated avalanche photodiode (eAPD) SAPHIRA detector, described in detail in Finger et al. (2012). This technology offers an advantage over conventional EMCCD with super-fast readout (1750 fps) and subelectron readout noise. The detector consists of 320x256 eAPD pixels, each $24\mu m$ in size and covering an on-sky area of 0.07 arcsec per pixel.

The C-RED is the camera that will ultimately be used on the completed AGWS instruments on the GMT for the J-band phasing observations (Kopon et al. 2018). Its fast, low-noise readout will permit the fringes to be observable without atmospheric blurring. Current testing has been performed with the Ninox VIS-SWIR 640 due to an issue with the C-RED power source. Testing with the Ninox may limit the fringe resolution, so tests with the C-RED will be necessary to measure if this setup is sufficient to determine if we meet the WFPT requirements outlined in McLeod et al. (2021).

This DFS prototype was the topic of a previous senior thesis (Frostig 2018), including the development of analysis software for the fringes, the construction of part of the prototype, and tests of its throughput. Additional tests were performed on the Magellan Clay Telescope using this prototype.

Testing and Analysis

Using the simplified PTT array described in Section 2.2, we align the separation between the mirror facets with the gap between subapertures, as seen in Figure 2.17 To analyze the fringe images, we Fourier transform the region of interest and take the absolute value. Shears in the fringes correspond to translation of the sidelobes in the Fourier

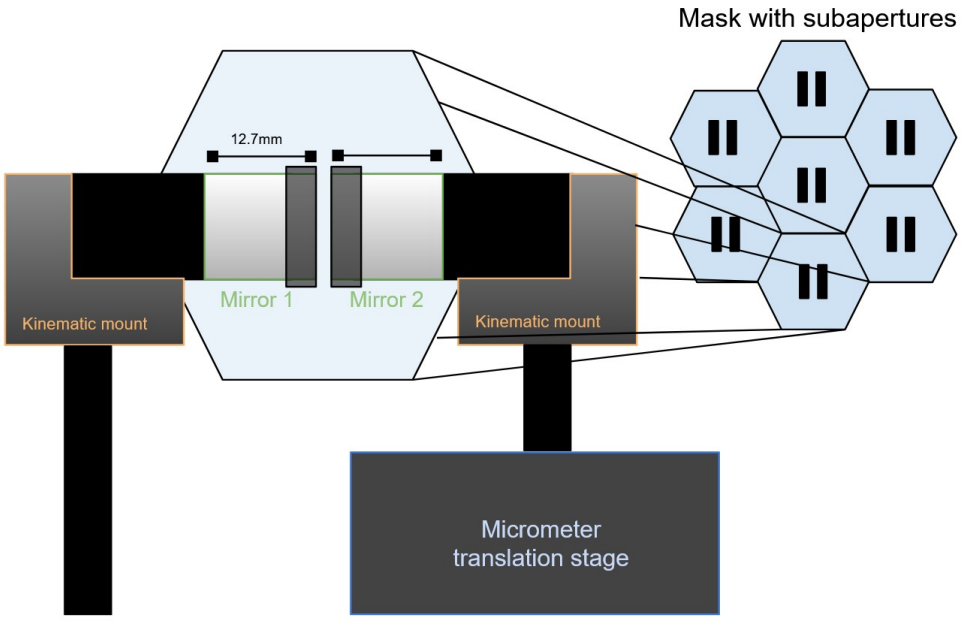

Figure 2.17: Simplified piston-tip-tilt mirror array with DFS mask and subapertures shown.

transformed image, and this translation relates linearly to the piston phase displacement. The analysis code was written as a part of Frostig (2018) and modified by the author of this thesis. Science images are crosscorrelated with simulated images, and the location of the sidelobe is measured with a quadratic fit, which provides an estimate of the piston phase difference. This code works on images with vertical subapertures, which requires rotating the images before processing. This is easily accomplished using the scipy Python package.

Results

The dispersed fringe sensor was tested by aligning the mirrors in tilt using the SHWFS and then taking images while recording the location of the micrometer corresponding to each image. This allows us to compare the calculated piston displacement from the software described in Section 2.3.2 and compare it to the measured value from the translation stage's micrometer. The results of this testing from three different data sets are shown in the Appendix (chapter 5). The differences between the values read off the micrometer and the piston displacements calculated by the software are moderately large, with values from 0.16μm to 4.11μm. It is likely that this is caused by inaccurate micrometer readings due to its coarse scale (each marking on the micrometer corresponds to 10μm of translation). The piezo-actuated PTT arrays will have much more precise control over the mirrors' positions than the manual micrometer on the translation stage provides.

Additionally, one of the primary aims of this project is to determine the precision to

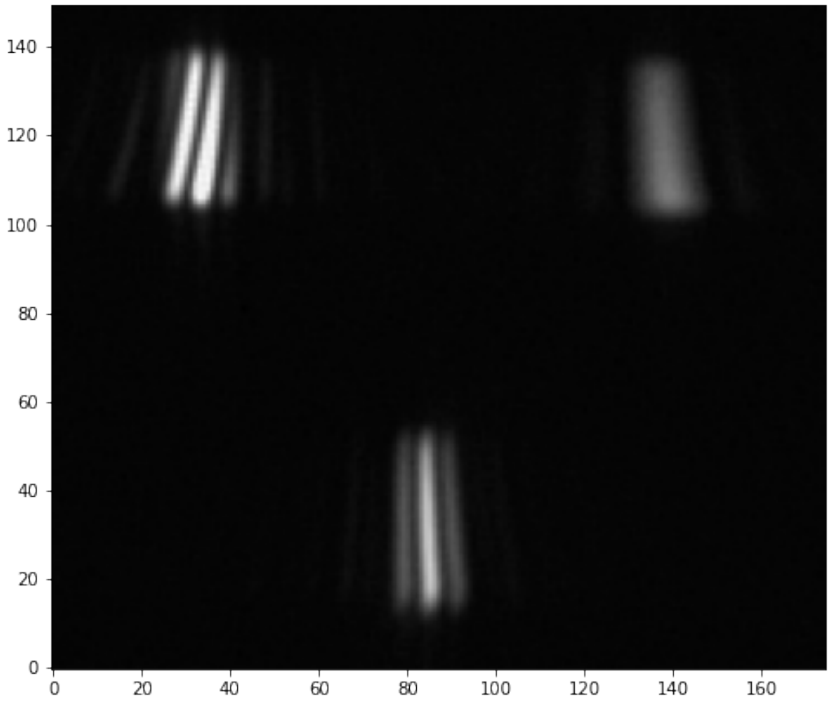

Figure 2.18: Sample dispersed fringe sensor image. Axes are in pixels. Tilted fringes in upper left are from subaperture spanning mirror gap.

which our sensor can measure the piston displacement. We collect 15 1100ms exposures over a fifteen minute period using the preliminary two-mirror prototype without adjusting the mirror positions. Analyzing the subaperture that spans the mirror gap demonstrates the significant drift measured by the DFS over this period of time - roughly 600nm of travel. When we instead measure a subaperture that does not span the mirror gap, we find a standard deviation of the calculated piston values of 63 nm. This provides a measure of the system's precision. The drift of this prototype is not a concern as the design differs significantly from the final piezo-actuated design. This value of 63nm is significantly smaller than the assembly tolerance for the PTT of 7.1μm, indicating that our setup is sufficiently precise to measure the required piston displacement. (See Section 2.4 for a discussion of the piezo-actuated two facet prototype results.)

The DFS analysis code can analyze a single image to calculate the piston displacement in 1.5 ms and a batch of 15 images in only 4.5 ms. Compared to the exposure time of 1100ms used in these tests, we can therefore analyze data much faster than it is obtained. In final testing of the DFS, 10 ms exposures will be taken and averaged every 30s. This code is sufficiently fast to analyze each individual exposure, not including the time to save the large data files.

2.4 Piezo Actuated PTT array Prototype Results

The piezo-actuated two-facet PTT array prototype was completed in March of 2021. The existing SHWFS and DFS setup and software was used to analyze its performance.

Figure 2.19 shows a comparison between reference fringes showing only one mirror facet (and therefore no phase difference) and fringes from the subaperture spanning the

mirror gap. Analysis as described in Section 2.3.2 yields a phase difference of 2.8 microns. Analyzing a DFS image with no segment gap provides a piston value of 0.07μm, or 70nm, and we take this as a first estimate of the precision of the setup. This is in approximate agreement with the precision estimated using the simplified PTT of 63nm. Both of these values are significantly smaller than the assembly tolerance for the final PTT array, and therefore indicate that the DFS is sensitive enough to assemble the PTT.

Figures 2.20, 2.21, and 2.22 show Shack-Hartmann wavefront sensor images of the prototype with one volt in each of the actuators. These images allow us to determine the effect of each actuator individually and use this to correct for tip-tilt differences in upcoming tests.

Additionally, overnight stability data was taken along with simultaneous temperature data. The SHWFS results from this are shown in Figure 2.23. This shows that temperature is likely the dominant source of tilt change over time. The RMS value of the fit was 0.17 pixels, which corresponds to a tilt difference of 0.05 mrad, which is significantly smaller than the tilt value produced by the 7.1 μm assembly tolerance for the PTT (0.88mrad), meaning that we again find that the setup is sufficiently sensitive. Correcting for the strong temperature dependence seen in Figure 2.23 yields Figure 2.24. We find an RMS wavefront error of 15.7nm, which is significantly smaller than the wavelength used for analysis and significantly smaller than the 7.1μm assembly tolerance of the PTT prototype.

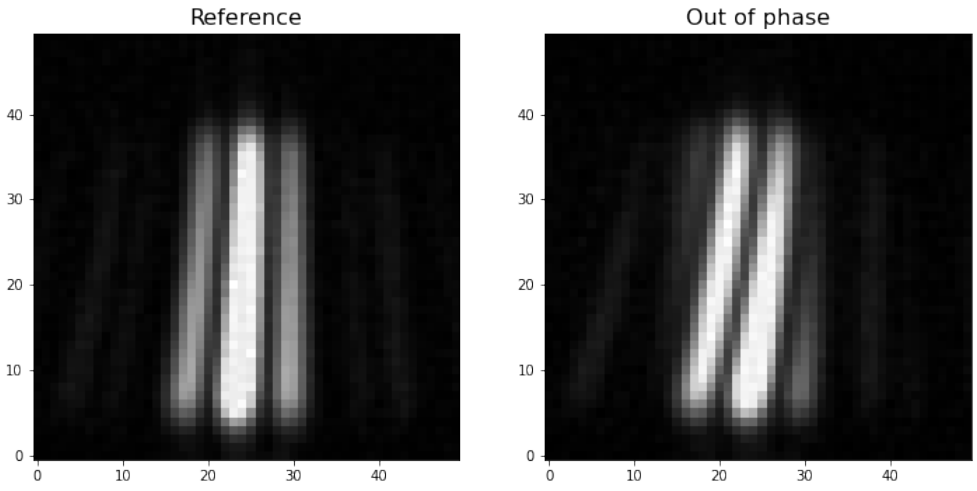

Figure 2.19: Dispersed Fringe Sensor images of piezo-actuated two-facet PTT array. Left panel shows unsheared fringes, right panel shows fringes that are tilted due to a 2.8μm phase difference.

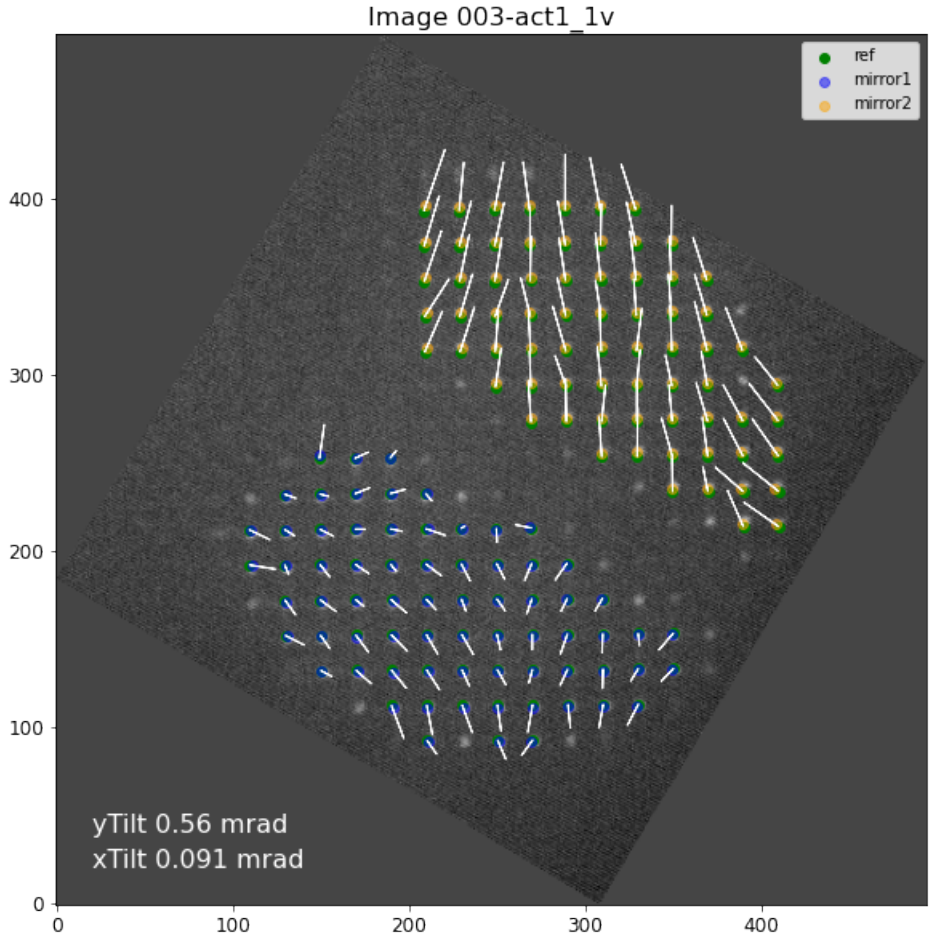

Figure 2.20: Shack-Hartmann Wavefront Sensor image of two facet PTT array, with 1 volt imparted on actuator 1.

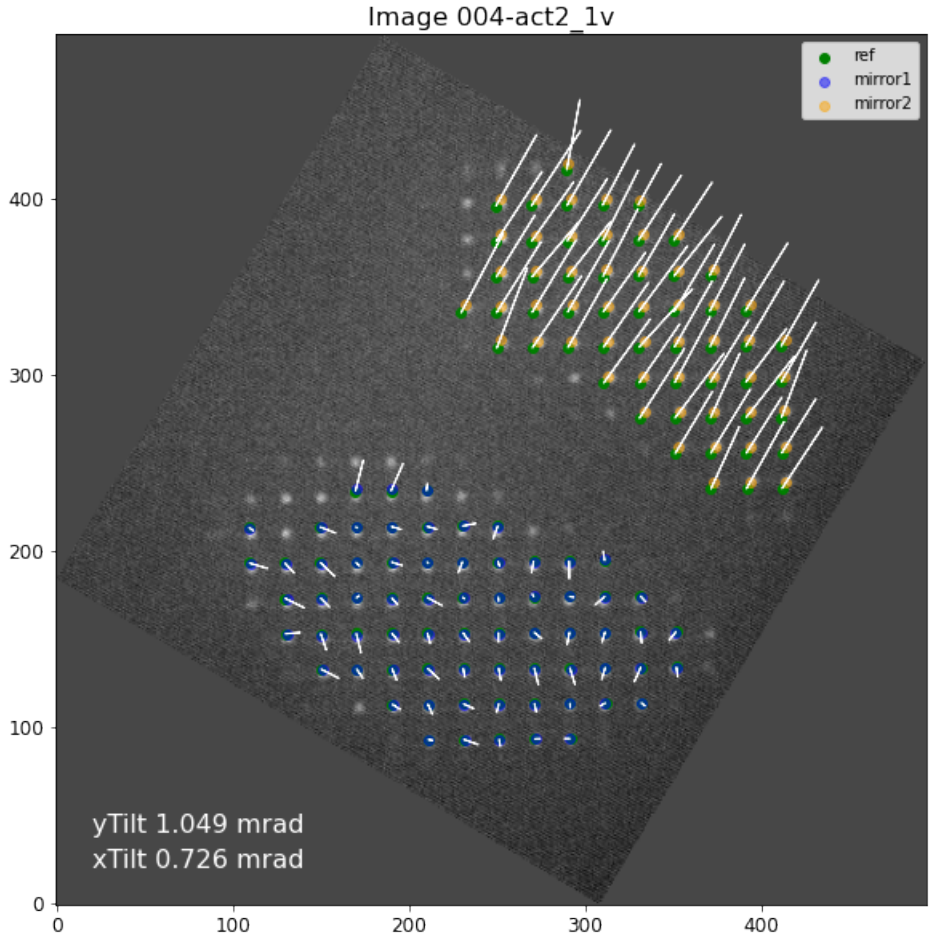

Figure 2.21: Shack-Hartmann Wavefront Sensor image of two facet PTT array, with 1 volt imparted on actuator 2.

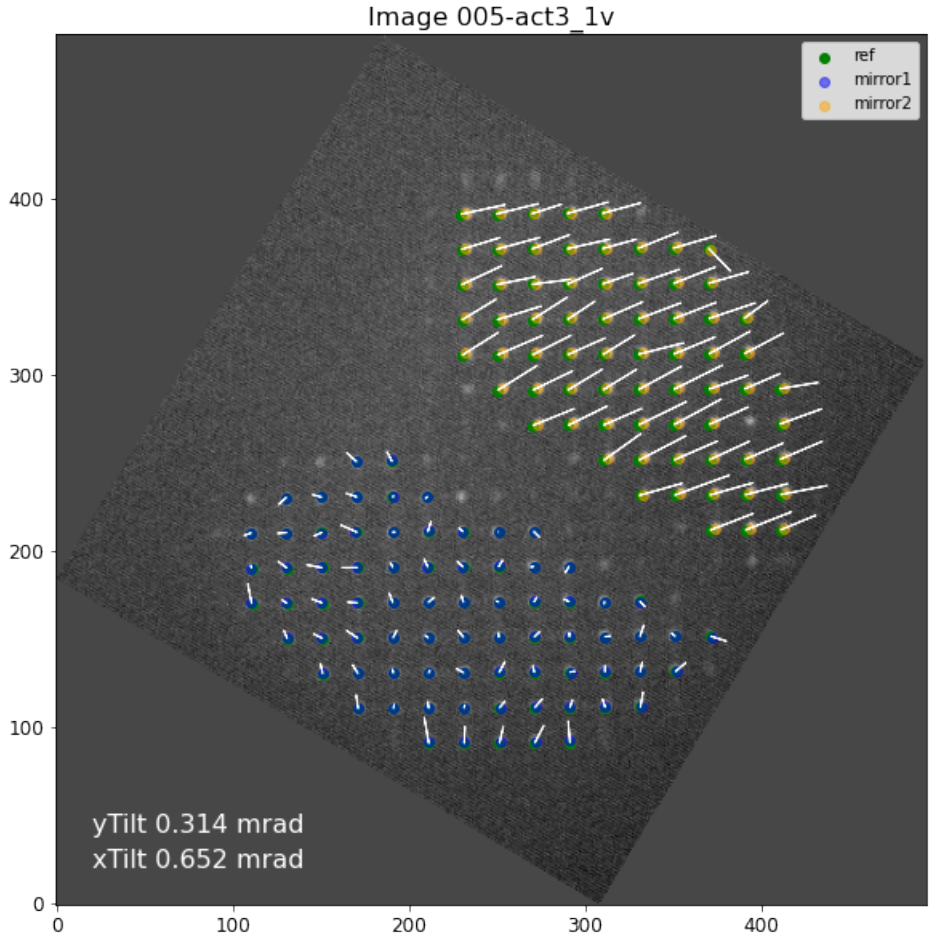

Figure 2.22: Shack-Hartmann Wavefront Sensor image of two facet PTT array, with 1 volt imparted on actuator 3.

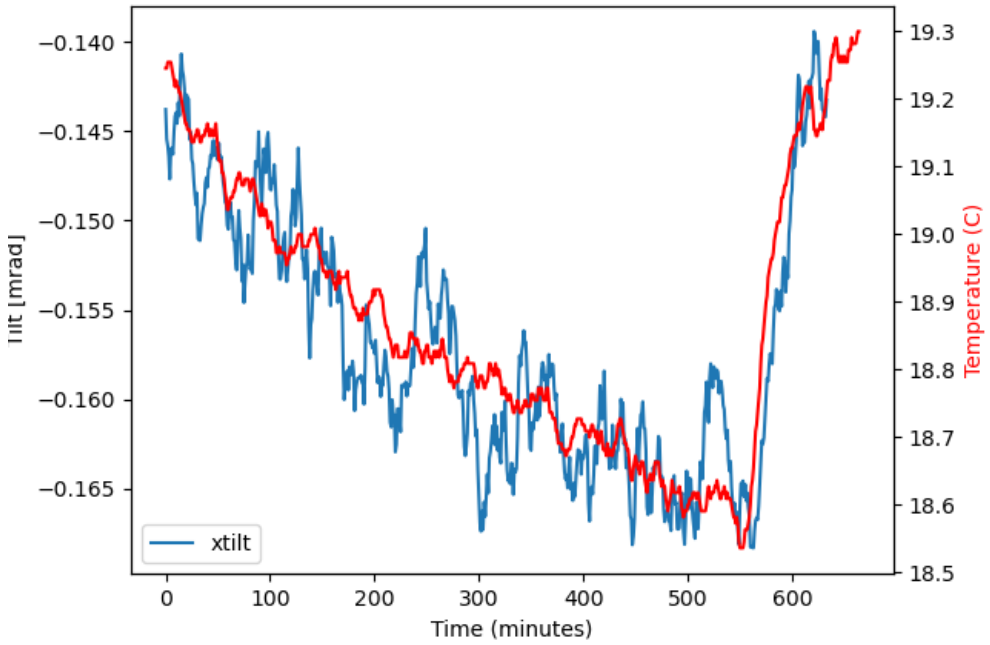

Figure 2.23: Overnight SHWFS stability data of the two-facet piezo actuated prototype. X Tilt values shown in blue, lab temperature shown in red. (Note: X and Y tilts are highly correlated, similar trend applies to Y tilt.)

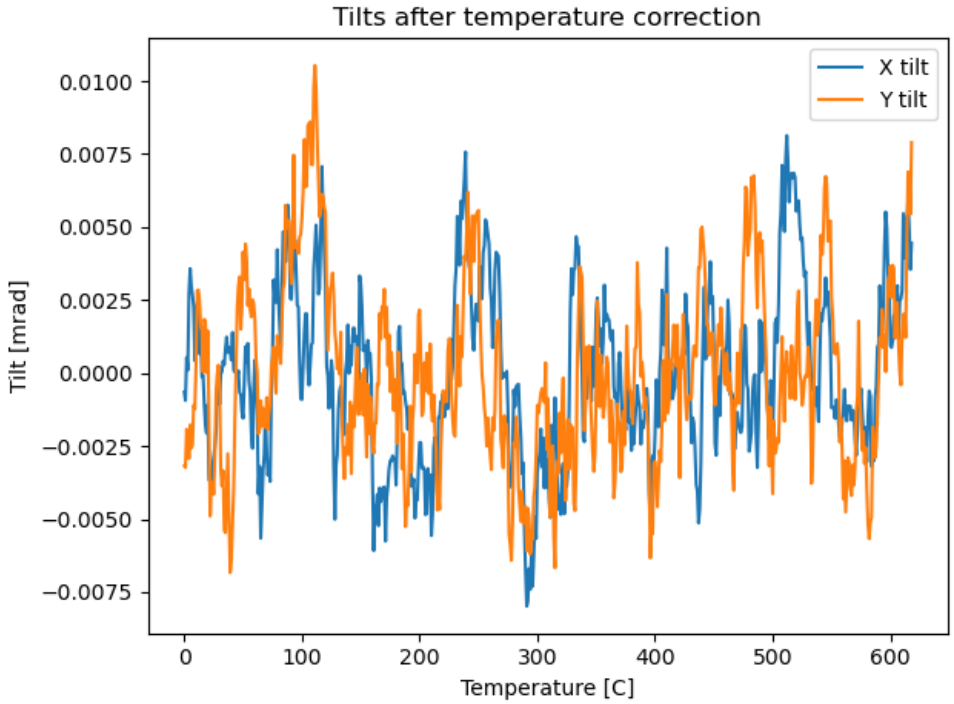

Figure 2.24: X and Y tilt values from SHWFS stability data of two-facet piezo actuated prototype after correcting for temperature trend.

Chapter 3

Alignment and Mirror Placement

3.1 Background

The WFPT is a complex optical setup with many intermediate conjugates. The AGWS team determined that an optic-by-optic sequential alignment is preferable to an end-to-end single-step alignment, because it is deterministic, less sensitive to false solutions from misalignment between relay sections, and allows us to investigate the wavefront behavior on individual relays. To enable precise alignment of the Wide-Field Phasing Testbed, we use a Leica laser tracker (LT) and a 4D Technology PhaseCam 6000 Dynamic Interferometer.

Off-axis parabolic mirrors are used throughout the design to relay the beam through the phase plates, to direct the beam off of the piston-tip-tilt mirror arrays and deformable mirrors, and to create the output relay with the appropriate focal distance. Because the full WFPT design contains 8 pairs of off-axis parabolic mirrors, it is crucial for us to be

able to align them within the assembly tolerance allotted for in the design.

3.1.1 Off-Axis Parabolic Mirrors

Off-axis parabolic mirrors (OAPs) are a key component of the larger WFPT design (see Section 1.3 and Figures 1.5 and 1.6), used to reflect the beam between the relevant optical elements without introducing chromatic aberration. OAPs have the unique advantage that the optical path length of all rays are equal. This also leads to the image (focal) plane of an OAP being a curved surface. OAPs are characterized by their diameter, their effective (or reflected) focal length, and their angle. Their geometry is shown in Figure 3.1.

In the full WFPT design, six pairs of OAPs are used to create a reflective design that compactly maintains image quality. The optical design using OAPs can be seen in Figure 1.5. To preserve image quality, the OAPs must be aligned correctly, within the allotted design tolerance of 3 arcminutes. This will be accomplished using the laser tracker and interferometer described in sections 3.1.2 and 3.1.3.

3.1.2 Laser Tracker

The laser tracker (Leica Absolute Tracker, model AT402) used in these experiments is a precise and portable laser tracker, shown in Figure 3.2. It has a typical resolution of $0.05\mu m$, a typical accuracy of $\pm 5\mu m$, and a typical repeatability of $2.5\mu m$ (Hexagon 2013). At the time of its release it was the most accurate laser tracker on the market. The laser tracker is used with spherically-mounted retroreflectors (SMRs). SMRs return

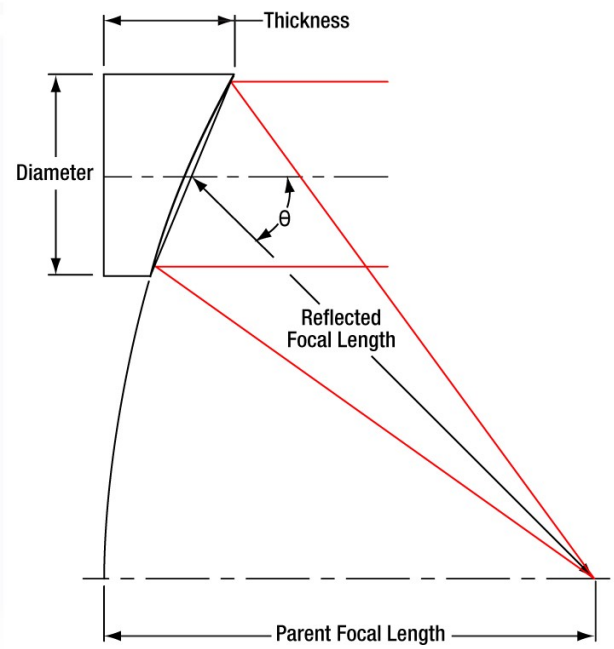

Figure 3.1: A diagram showing the key parameters that describe an off-axis parabolic mirror. Figure reproduced from ThorLabs.com.

the beam to the laser tracker and allow it to compute the distance between the tracker and the target SMR. The Leica AT402 has Powerlock, which enables the laser beam to automatically search for, move to, and lock onto an SMR (Hexagon 2013). An SMR is shown in Figure 3.3, measured both directly and in reflection. Measurement through reflection is described in more detail in Section 3.3.

3.1.3 Interferometer

The 4D Technology PhaseCam 6000 Dynamic Interferometer is a compact laser Twyman-Green interferometer that uses a single camera, high-speed optical phase sensor to take measurements in $< 30\mu s$ (4DTechnology 2017). This very short timescale allows the observations to not be affected by vibration and turbulence. It has a small field

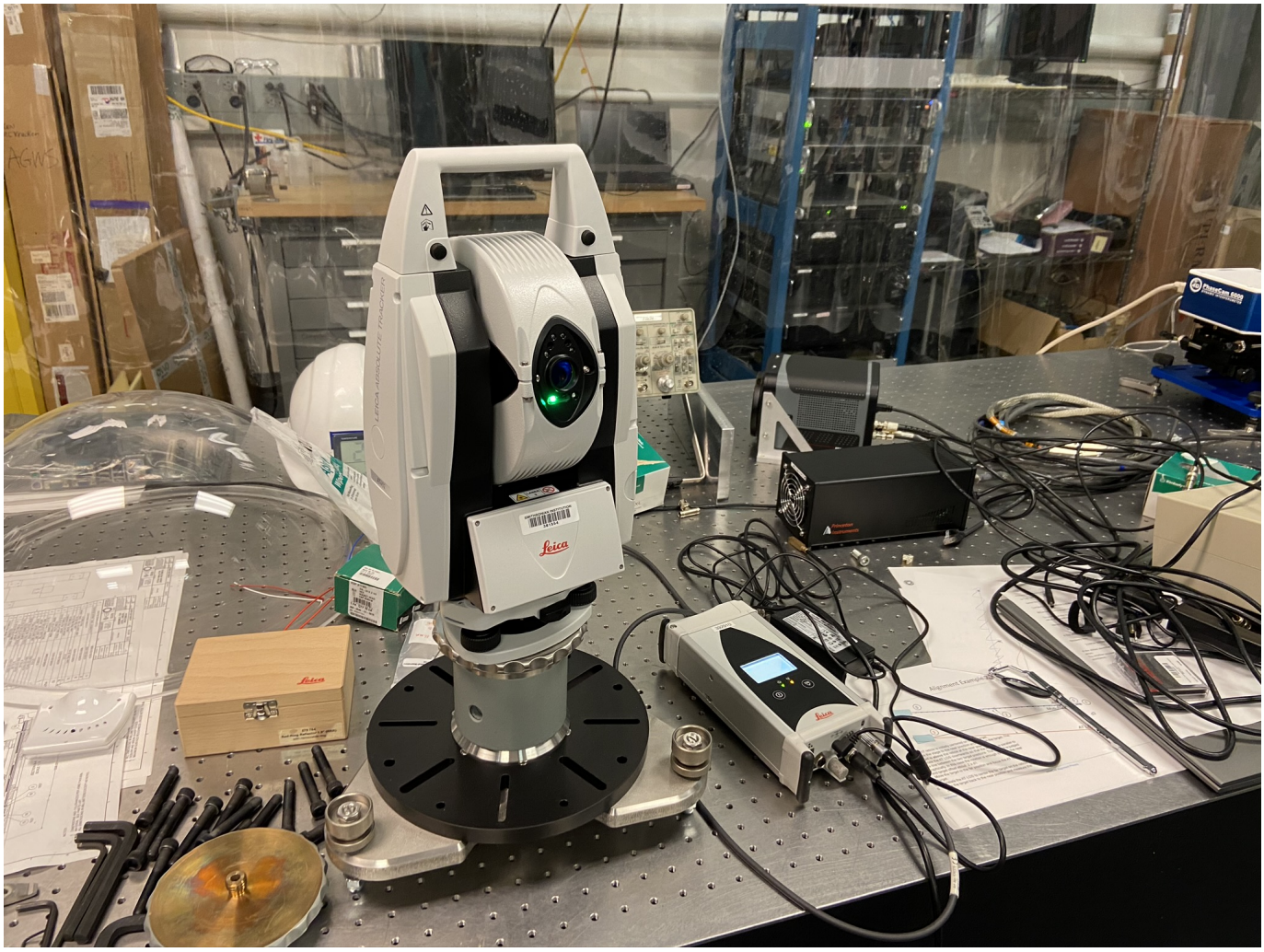

Figure 3.2: Leica Absolute Tracker AT402, pictured on the optical bench in the lab.

of view ($8.95mm$) and a beam diameter with a full-width at half maximum of $9mm$ (4DTechnology 2017). Its laser operates at a wavelength of $\lambda = 632.8$ nm (4DTechnology 2017).

Twyman-Green interferometers are used to measure the surface shape and the wavefront quality off a variety of optical components. The interferometer used in these experiments uses quarter wave plates to polarize the signal, producing a phase shift that creates 4 distinct frames that are simultaneously captured by the camera. This is shown in Figure

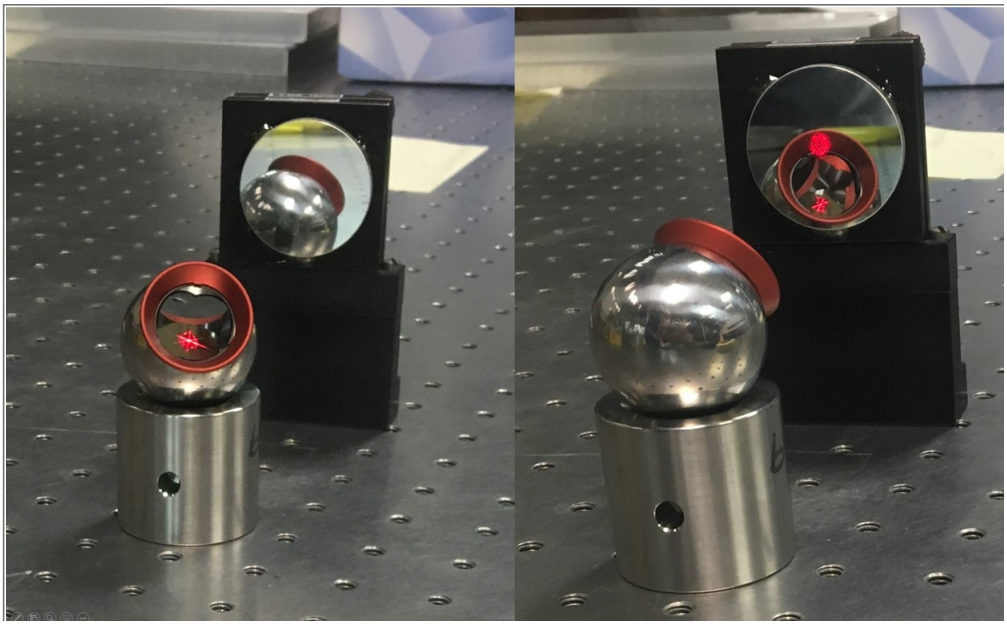

Figure 3.3: A spherically-mounted retroreflector (SMR) in its nest, shown both in direct measurement by the laser tracker (left), and in reflection (right).

3.4.

3.2 Specifications and Parts

Preliminary Testing

For the preliminary testing that comprises this thesis, we use 2 Edmund Optics OAPs with a diameter of 76.2mm, an effective (or reflected) focal length of 516.8mm, and an angle of 15°. The OAPs are mounted as shown in Figure 3.5. The mount used (Newport U300-AC2K) has tip-tilt adjustments with a range of ±3.5°, and is specifically designed to avoid aberrations that can arise from an optic being compressed by the set screws used in other mounting designs. The XYZ translation stage (Newport 9064-XYZ) has

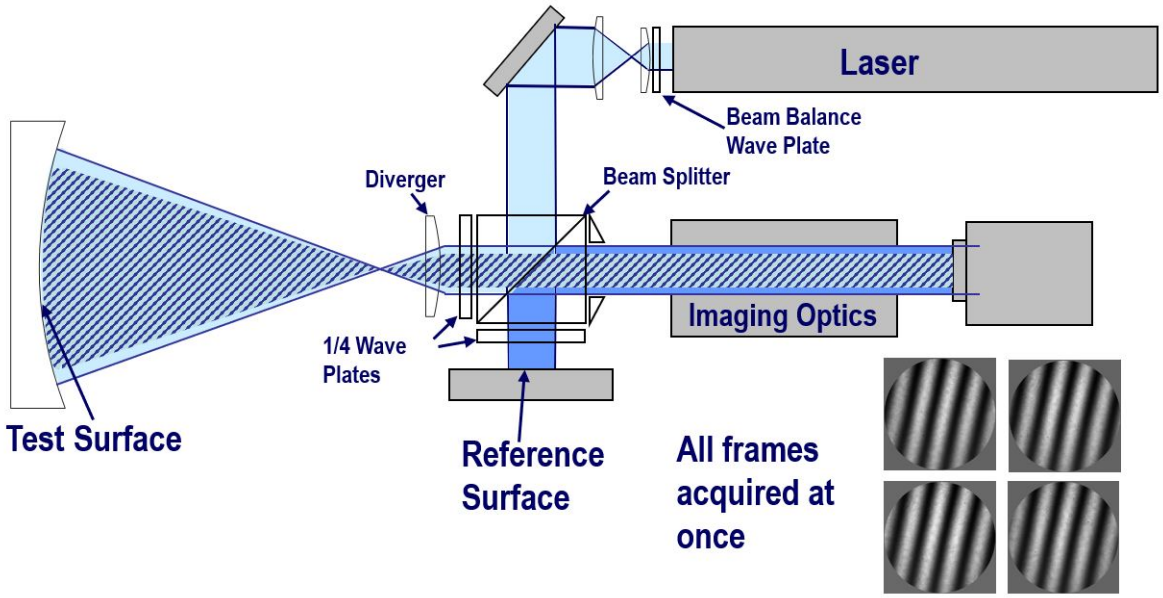

Figure 3.4: A Twyman-Green interferometer as implemented in the PhaseCam 6000. Figure reproduced from 4DTechnology (2021)

15.8mm of translation in each direction and is driven by actuators with a sensitivity of 0.71μm per degree.

Main Testing

In the full Wide-Field Phasing Testbed design, there are 3 OAP-based relays; two using mirrors with a diameter of 76.2 mm with a 24.5 mm pupil, and one using mirrors with a diameter of 101.6mm and a 51mm pupil. They will be mounted in the size-appropriate Newport Ultima series mount, as described above, providing $\pm 3.5°$ of tip-tilt adjustment and preventing aberrations due to mount pressure. This will be affixed to a Newport 9064-XYZ translation stage as in the preliminary tests.

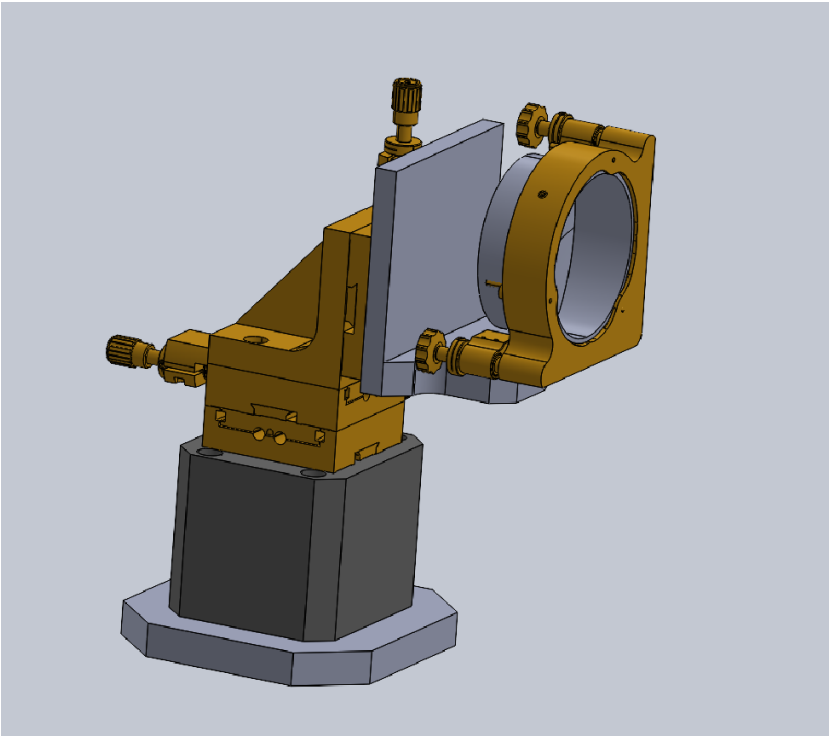

Figure 3.5: Mounting configuration for a 76.2mm-diameter off-axis parabolic mirror. Off the shelf parts are shown in gold and machined parts are shown in grey.

3.3 Method

We must first establish a bench coordinate system, which is accomplished by measuring the locations of three 0.5" spherically-mounted retroreflectors (SMRs) which are secured to the bench semi-permanently.

3.3.1 Laser Tracker Placement of Flat Mirrors

If the reflection of an SMR is returned to the laser tracker via a flat mirror, it will instead measure the virtual image (VI) position. (This is diagrammed in Figure 3.6.) This is the crucial property of the LT we will use to place and align the optical components of our

system. Equations 3.1-3.3 define the virtual image position $\vec{V}$ based on the measured SMR position $\vec{R}$,the fiducial position of the mirror $\vec{M}$, and the mirror's fiducial normal vector $\vec{N}$.

$$\vec{R} - \vec{M} = \vec{d} \tag{3.1}$$

$$\vec{d} \cdot \vec{N} = m_N \tag{3.2}$$

$$\vec{V} = \vec{M} - 2m_N\vec{N} \tag{3.3}$$

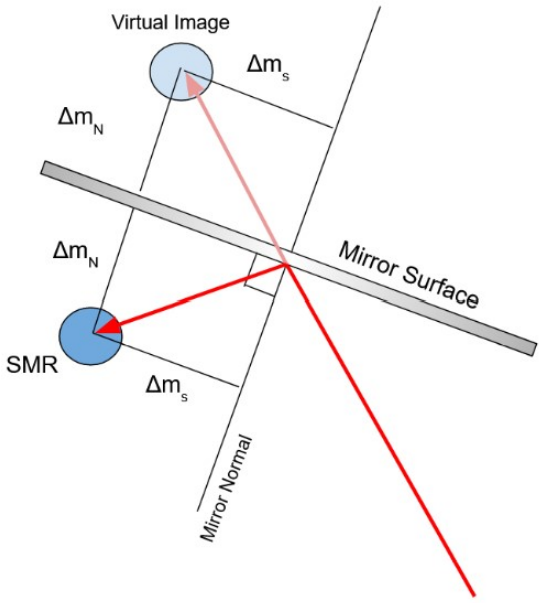

Figure 3.6: Use of a flat mirror and SMR to measure the virtual image position. Laser tracker beam shown in red; with the path to the virtual image shown in a lighter shade.

3.3.2 Alignment Procedure

An alignment methodology has been outlined by the AGWS team and is described in McLeod et al. (2021). This alignment is performed one optic at a time, sequentially, which minimizes risks associated with end-to-end alignment. Their plan involves using spherically mounted retroreflectors (SMRs) located at the object and focal positions and measured with the laser tracker (Leica AT402, as described in Section 3.1.2.)

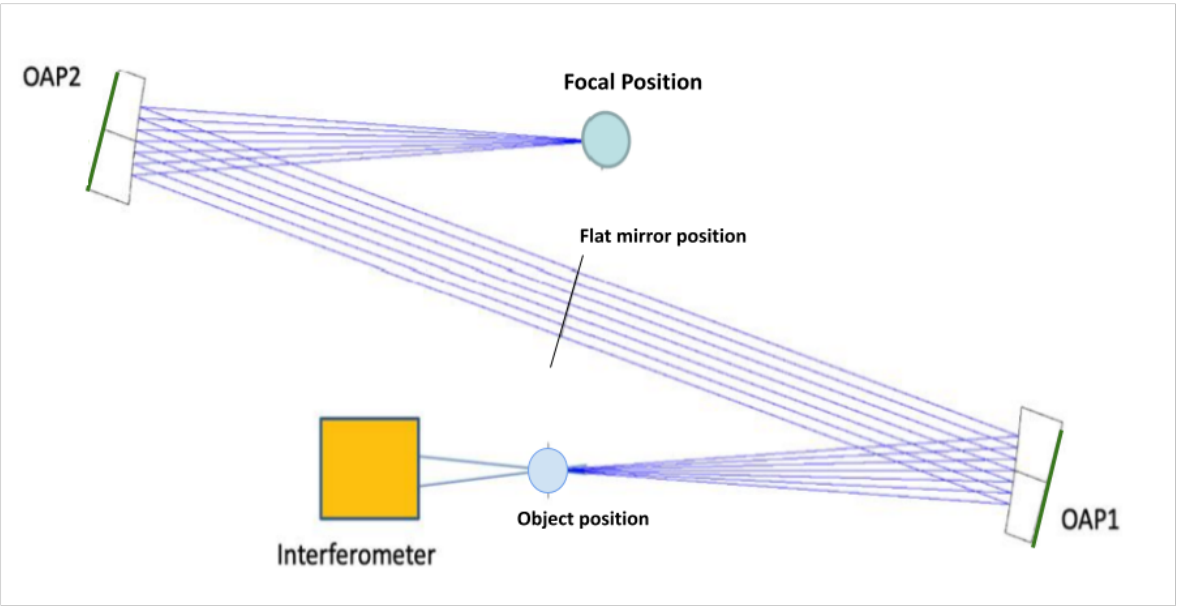

Figure 3.7: Diagrammed alignment setup for one pair of off-axis parabolic mirrors using the laser tracker and interferometer. Reflective back surfaces of the OAPs used for tilt alignment are shown in green.

An interferometer (the PhaseCam 6000, as described in Section 3.1.3) will be used and aligned until the fringes from the reflection off the SMR null out, meaning that the reflection off of the test surface is focused at the same location as the incoming interferometer beam. The tilt of the OAP mount will be set using the back surface of the

OAP which is covered with a reflective coating. The OAP will then be translated to null out the return on the interferometer. This will be repeated for each subsequent pair of OAPs. The full alignment will occur after this thesis' completion, but we align one pair of OAPs, and therefore set the procedure to be used on subsequent pairs. In subsequent figures, C1 denotes the focus location.

Step 1: To align a single pair of OAPs and a flat mirror, we must begin with an SMR on a 3-axis translation stage located at the object position. (It will be positioned to within $5\mu m$ accuracy using the laser tracker.) Then we null out the interferometer reading, using the shiny surface of the SMR as the source. (See Figure 3.8)

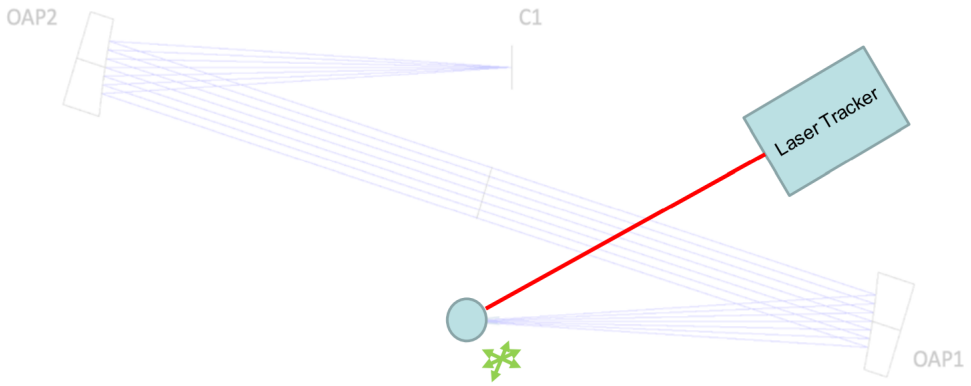

Figure 3.8: Alignment Step 1.

Step 2: We then place the first flat mirror at its approximate location and record the position of the SMR as measured directly (not through reflection), as seen in the left panel of Figure 3.3. Using the software described in the next section, we compute the virtual image position if the flat mirror was in its prescribed location. We then shift to

observe the SMR via reflection, as seen in the right panel of Figure 3.3, and adjust the mirror position and tilt until the laser tracker measured virtual image position matches the coordinates output by our software. To reduce the degeneracies between adjustments made on the mirror mount, the laser tracker is aligned so that its beam is roughly parallel to the mirror normal vector, decoupling changes in distance, vertical angle, and horizontal angle. (See Figure 3.9)

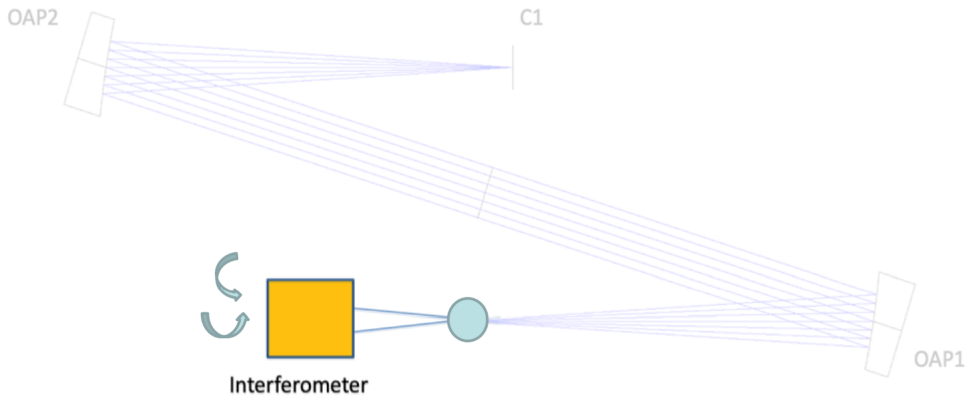

Figure 3.9: Alignment Step 2.

Step 3: We use the reflective back surface of the OAP in its mount to position the tip/tilt of the OAP using the laser tracker, again by comparing the real measured nest position to the virtual image position that would be measured if the mirror was in the position specified in the Zemax file. (See Figure 3.10)

Step 4: Once the tilt of the OAP has been set, it will be translated (without affecting the tilt) to null out the interferometer. (See Figure 3.11)

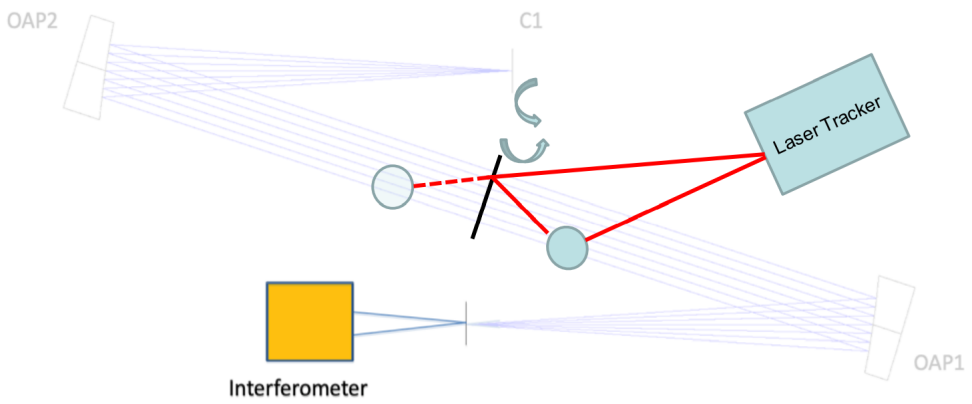

Figure 3.10: Alignment Step 3.

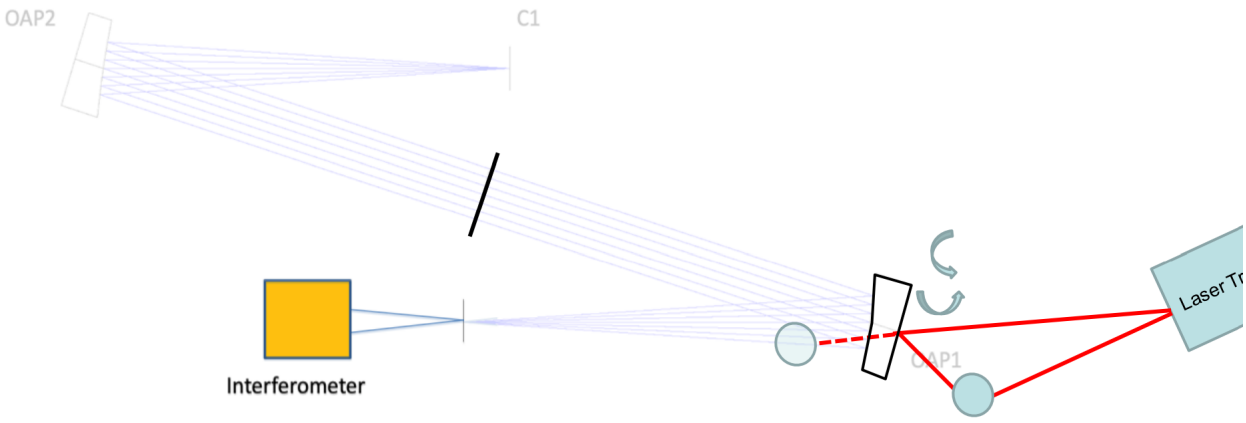

Figure 3.11: Alignment Step 4.

Step 5: The laser tracker is then used to position an SMR at the next object position. (See Figure 3.12)

Step 6: The laser tracker is to set the tip/tilt of the second mounted OAP, again by

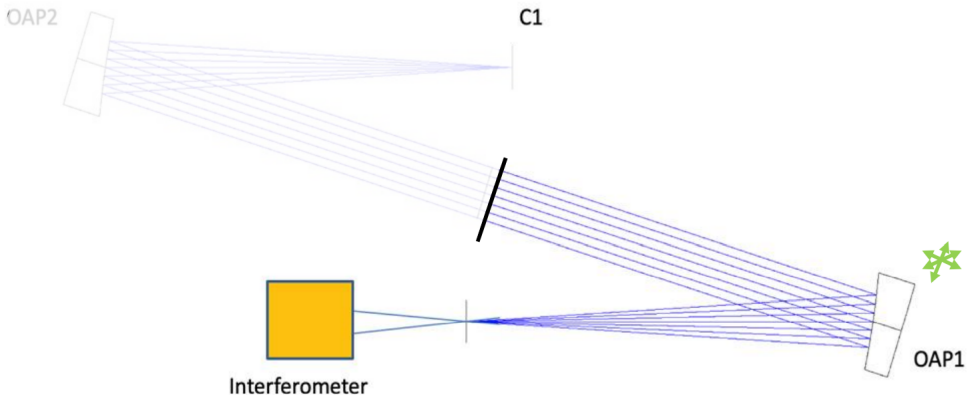

Figure 3.12: Alignment Step 5.

comparing the real measured nest position to the virtual image position that would be measured if the mirror was in the position specified in the Zemax file. (See Figure 3.13)

Step 7: Finally the second OAP will be translated (without changing the tilt) to null

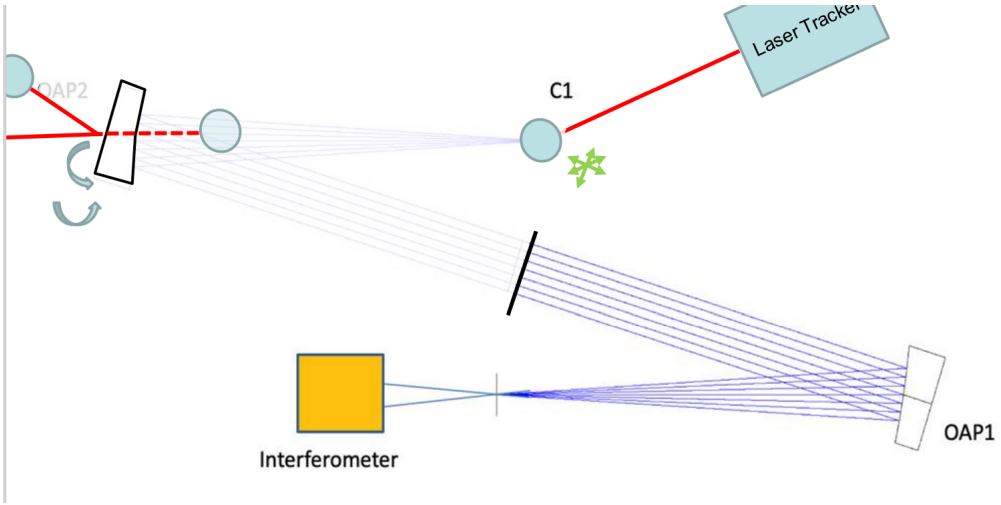

Figure 3.13: Alignment Step 6.

out the interferometer. This leaves the pair of OAPs aligned. Figure 3.7 shows the object, OAP, flat mirror, and final positions. (See Figure 3.14)

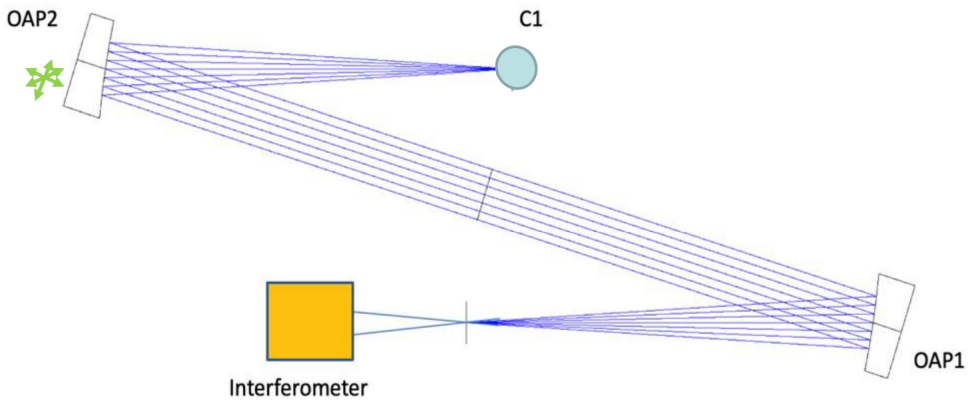

Figure 3.14: Alignment Step 7.

Figures 3.15 and 3.16 show interferometer measurements of the SMR surface. As discussed in Wyant (2016), the four simultaneous interferograms acquired in phase-shifting interferometry, like that done by the PhaseCam used in this project, can be analyzed to yield the height error as a function of image coordinates as follows. Equation 3.4 provides the formula to calculate the measured object phase ($\phi(x, y)$) from the intensity maps of the four simultaneous images (I_1, I_2, I_3, I_4). Equation 3.5 converts this to a height error ($H(x, y)$) using the wavelength of the interferometer (λ).

$$\phi(x, y) = \arctan\left(\frac{I_4(x, y) - I_2(x, y)}{I_1(x, y) - I_3(x, y)}\right) \tag{3.4}$$

$$H(x, y) = \frac{\lambda}{4\pi}\phi(x, y) \tag{3.5}$$

Reanalyzing the images in Figures 3.15 and 3.16 using equations 3.4 and 3.5 yields 2D

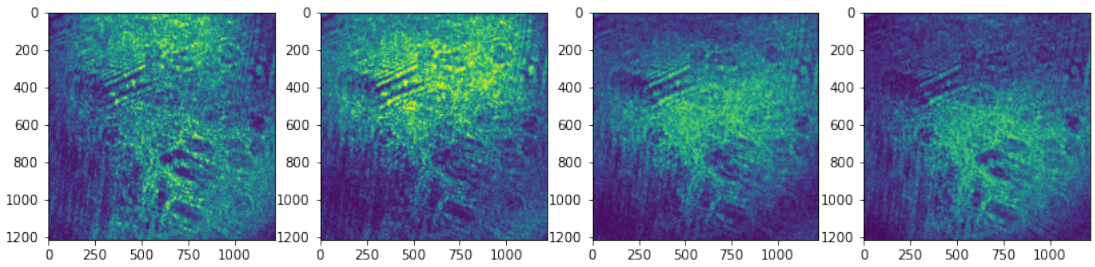

Figure 3.15: Interferometer images of the SMR surface when the system is positioned to eliminate all interference patterns, also known as 'nulled out'. The four frames are taken simultaneously.

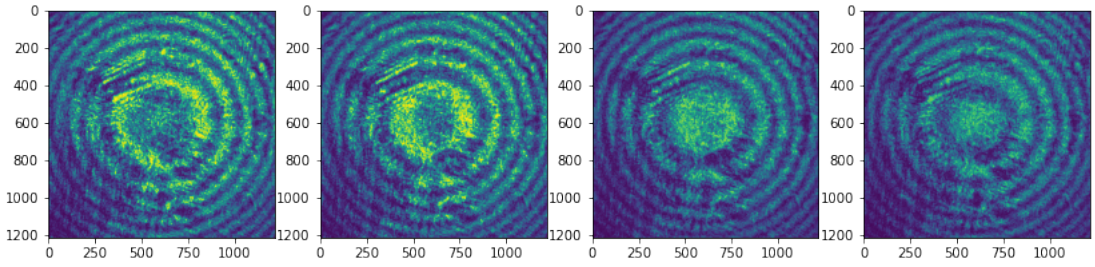

Figure 3.16: Interferometer images of the SMR surface showing the interference patterns that indicate the system is not correctly positioned. The four frames are taken simultaneously.

maps of height error, shown in Figures 3.17 and 3.18. Using the interferometer allows us to investigate the shape of the wavefront and determine if its beam is focused at the correct location. More in-depth characterization of the interferometer performance may be required at a later date.

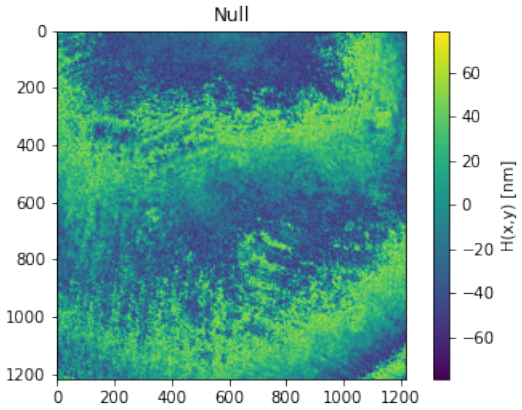

Figure 3.17: Height error of the SMR surface as a function of image coordinates, created from the 4 phase shifted frames shown in Figure 3.15.

3.4 Software

The first goal of our software is to convert between the bench coordinate system, the laser tracker native coordinate system, and the coordinate system exported from a Zemax optical design file. Additionally, the laser tracker can perform measurements in either a Cartesian or spherical coordinate system, both of which are used in our procedure. We use Python to perform the coordinate transformations.

To convert between two Cartesian systems, one must know the origin of the new coordinate system as measured in the old coordinate system, and the unit vectors of the

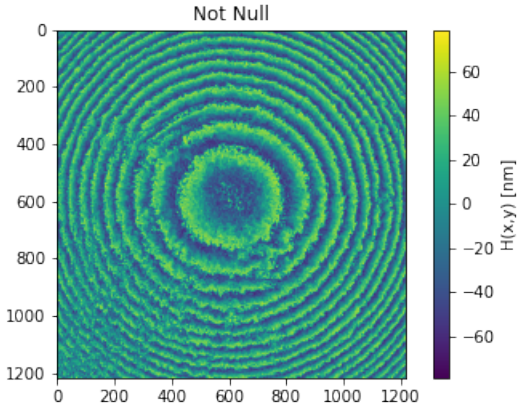

Figure 3.18: Height error of the SMR surface as a function of image coordinates, created from the 4 phase shifted frames shown in Figure 3.16.

new coordinate axes as expressed in the old coordinate system. Figure 3.19 shows the 3 Cartesian coordinate systems' unit vectors and the locations of the SMRs permanently affixed to the bench.

The second goal of our software is to perform the calculations necessary to place mirrors in the positions from the Zemax optical design prescription. This is accomplished in real-time in the lab.

We use the measured position of the SMR nest in the laser tracker coordinate system and the fiducial position and normal vector of the mirror surface in the Zemax coordinate system. We first convert these values to the bench coordinate system defined by the 3 SMRs permanently affixed to the bench, and then compute the component of the difference between the mirror and the nest that is in the direction of the mirror's normal vector (labeled Δm_N in Figure 3.6). We then use this to compute the expected virtual image position if the mirror was in the precise location specified by the Zemax optical design file. Maintaining the optical path from the laser tracker to the mirror to the SMR,

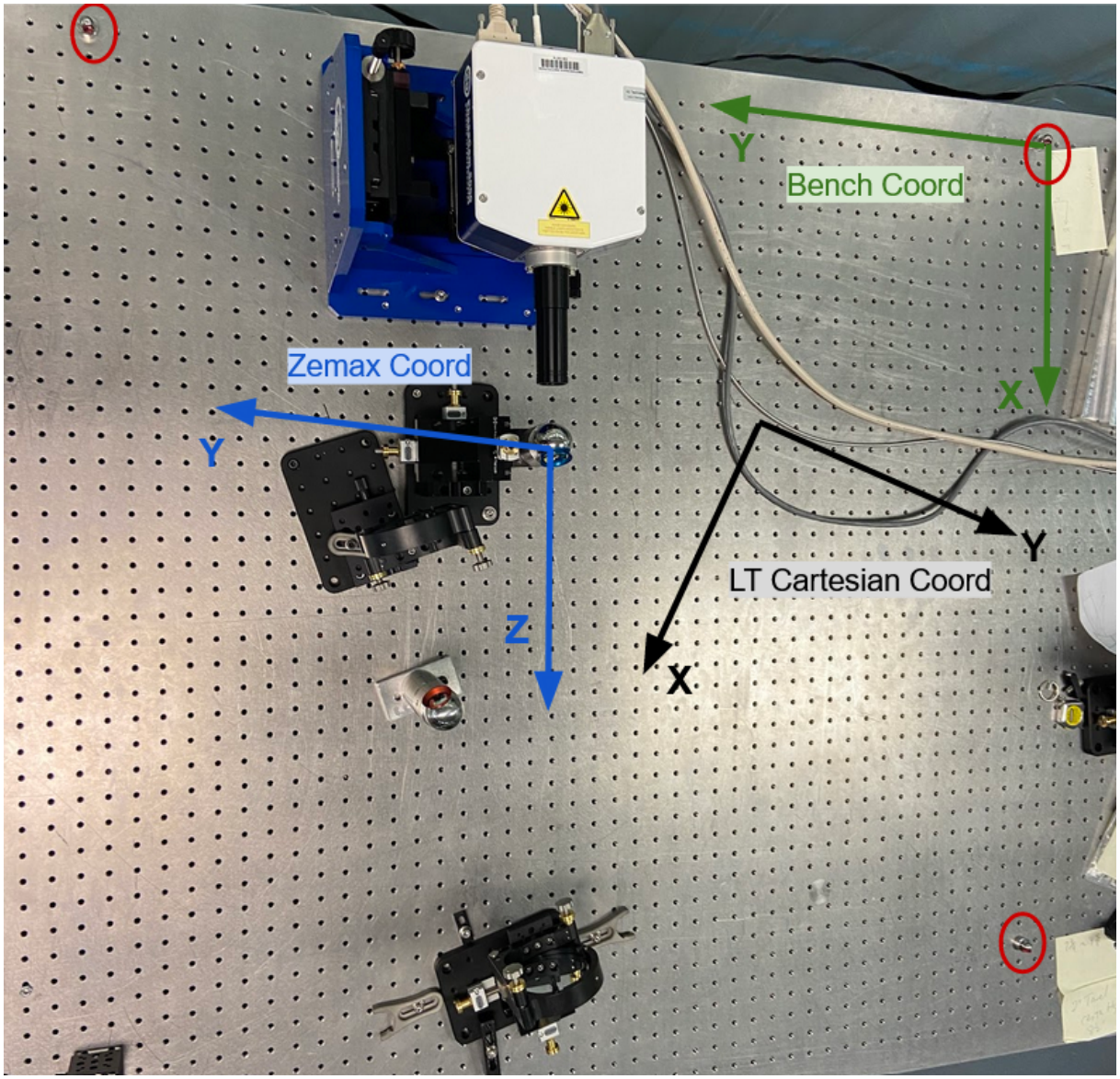

Figure 3.19: Bench used for alignment, shown with overlaid arrows representing unit vectors of each coordinate system placed at their approximate origin. Black arrows are from the laser tracker cartesian coordinate system, green arrows are from the bench coordinate system, and blue arrows are from the Zemax coordinate system. The 0.5" SMRs used to establish the bench coordinate system are circled in red.

we then adjust the mirror in position, tip, and tilt until the position the laser tracker measures matches the computed fiducial virtual image position.

This is accomplished via a 'measurement set' class in Python that records the positions of the bench SMRs to define the coordinate system and an additional SMR that's placed at the location corresponding to the Zemax coordinate system's origin. One can then choose the zemax surface corresponding to the optical element being placed and measure the direct position of the SMR. The software will then output the fiducial position of the virtual image calculated from the fiducial mirror position and the directly measured SMR position. If a virtual image measurement is taken, it can then be entered in as well and the software will report the 3D distance as well as the distances in the laser tracker's cartesian coordinate system. It can also report the difference between the mirror's fiducial normal vector and the normal vector of it's current position, calculated based on the measured real and virtual object positions.

3.5 Results

To analyze the accuracy and precision of the laser tracker measurements, we perform a repeated set of measurements. Each measurement set remeasures the location of the 3 permanent bench SMRs, the 'Zemax origin' SMR, and the direct and virtual image locations of the object SMR. The uncertainty on measurements of the bench and Zemax origin SMRs – which are not moved at all during the measurement process – is $3.84 \pm 0.92\mu$m. This value is nearly in agreement with the repeatability value reported by the manufacturer of 2.5μm. Early tests estimated the uncertainty on the position of the object SMR is 45.77μm and of its virtual image position is 68.71μm. This SMR must

be rotated back and forth to face the laser tracker (for direct measurement) and then to face the mirror surface (for VI measurement). This SMR is located on a fixed column that is clamped to the bench to prevent it from moving during adjustments; therefore it's reasonable to state that the larger errors on the direct and virtual measurements of the SMR position are due to slight aberrations in the spherical shape of the SMR resulting in a shift of the laser tracker's measured location after the SMR is rotated. However, repeating these tests with a higher quality SMR from a different manufacturer reduced the uncertainty on the directly measured position to 9.8 μm and on the virtual image position to 7.0 μm. Continued tests will use these higher quality SMRs. We estimate the uncertainty on the difference between the measured and ideal virtual image positions by summing the uncertainties of the object and virtual image positions in quadrature, which yields an uncertainty of 12μm.

The purpose of the SMR measurements is to allow us to correctly position the mirror surfaces at their locations and angles defined in the Zemax prescription. One measure of the success of this can be achieved by comparing the measured mirror normal vector to the fiducial mirror normal vector. In bench Cartesian coordinates, these vectors differ by averages of $(0.030 \pm 0.008\mu\text{m}, -0.34 \pm 0.09\mu\text{m}, 0.11 \pm 0.06\mu\text{m})$. To better quantify how well we are matching the mirror normal vector, we can compute the angle between our measured normal vector and the fiducial normal vector. The mean value of the angle between in repeated measurements is 1.17 arcminutes. In the iterative precision alignment process, we are consistently able to position mirrors such that the angle between the normal vectors is approximately 0.1 arcminutes.

In planning for the WFPT alignment, McLeod et al. (2021) allots for an error in mirror placement of 3 arcminutes, or 0.87 mrad. To determine if our measurements are

within this range, we consider the distance between the SMR and mirror surface and multiply by this angle to determine the maximum allowable linear error. In testing this setup, SMRs were placed roughly 200mm from the mirror surface. This corresponds to a linear error in placement of (200mm)(8.7×10^{-4}rad) = 0.175mm, or 175μm. Our measurements are significantly more precise than this, and therefore we believe that the current setup and measurement procedure is sufficiently sensitive to align the WFPT. The angular error of 3 arcminutes is larger than the angle between the normal vectors both in the repeated measurements (1.17') and in precise alignment testing (0.1'). Every step in the alignment procedure has been tested as a part of this thesis. Upon obtaining a return to the interferometer off of the flat mirror and the OAP in double-pass (as seen in Figure 3.12), a significant amount of astigmatism has been observed. This is apparent from the fringe patterns visible in Figure 3.20 and Figure 3.21. These patterns cannot be eliminated by translating the mirror as planned in the alignment procedure. Possible sources of this error include bending of the mirror from mounting, imperfect flatness of the flat mirror behind the OAP, or misalignment of the system as a whole. Ongoing and future experiments will be required to test each of these possible causes.

Our measurements of the laser tracker precision indicate that this procedure is sufficient to meet the specifications of the WFPT design as outlined in McLeod et al. (2021). Ongoing work will determine the optimal positioning of bench elements to ensure that the laser tracker maintains a clear line-of-sight to all the required optical elements, as well as measuring the errors associated with executing the full alignment procedure.

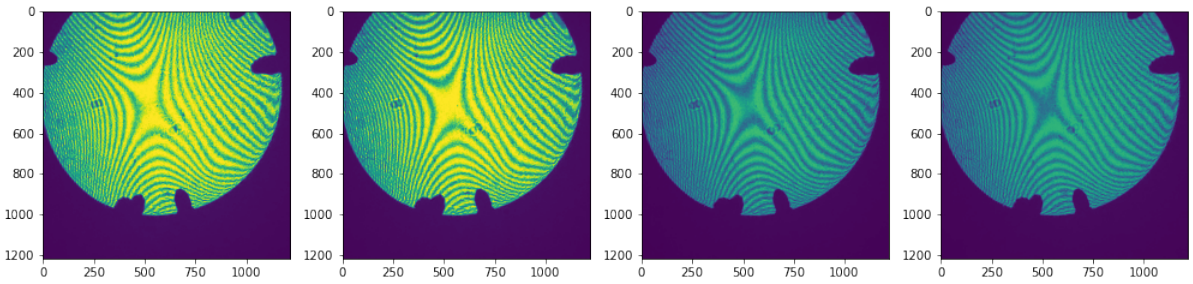

Figure 3.20: Interferometer images of OAP1, reflected off a flat mirror. Fringes indicate significant aberrations, the cause of which is not yet known.

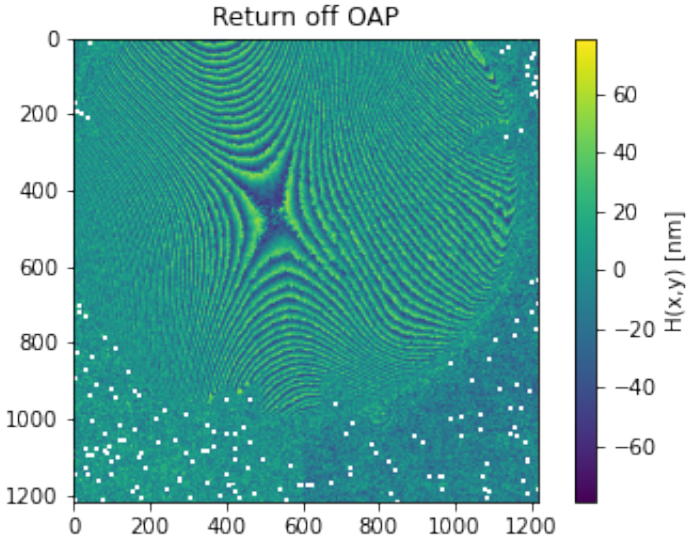

Figure 3.21: Height error of the OAP return beam as a function of image coordinates, created from the 4 phase shifted frames shown in Figure 3.20.

Chapter 4

Discussion and Conclusions

4.1 Summary of Results

In this thesis, we use a simplified two-facet piston-tip-tilt mirror array to test the sensitivity of two wavefront sensing prototypes. With the Dispersed Fringe Sensor (see Section 2.3.2), we have determined that the measurements of the facets' relative piston displacement are precise to 63 nm. We determined that the accuracy of our comparisons between the measured and calculated piston displacement values are likely limited by the coarse resolution of the readings on the translation stage's micrometer, which was resolved by the completion of the piezo-actuated mirror array. We successfully measured piston differences as large as 15μm. Using the Shack Hartmann Wavefront Sensor (see Section 2.3.1), we have determined that our measurements of the tilt difference between the mirror facets are precise to 0.082 mrad.

One primary goal of this thesis was to determine if the measurement setup is sufficiently precise to allow us to flatten the PTT array after its assembly. In the design of the

seven-segment piezo-actuated PTT array, 7.1μm has been allotted as the assembly tolerance. This corresponds to an angular displacement of 0.88 mrad, which is significantly larger than our SHWFS precision of 0.082 mrad. Our DFS measurements are precise to 63nm, which is much smaller than 7.1μm. This confirms that we have sufficient resolution in both tip/tilt as well as in piston displacement to verify the flatness of the final seven-segment PTT array.

The two-facet PTT array prototype was assembled in March 2021 and used for additional Shack-Hartmann and Dispersed Fringe Sensor testing as presented in Section 2.4. Overnight monitoring determined that temperature changes are highly correlated with the x and y tilt changes as measured by the SHWFS. Analysis of the PTT prototype is an ongoing effort of the AGWS team.

Additionally, this thesis tests the equipment required for successful alignment of the OAP relays involved in the full testbed design. We determine that the precision of the laser tracker measurements is affected by the rotation of the SMR even when it's atop a fixed mount, but this effect is drastically reduced by using a higher quality SMR. However, comparing the measured normal vectors to the normal vectors of the mirrors imported from Zemax optical design software, we determine that the alignment is sufficiently precise to match the design of McLeod et al. (2021).

4.2 Compliance with GMT AGWS Standards

The total WFPT will replicate additional properties of the true GMT optics that are not included in this thesis' work, including atmospheric turbulence and field dependent aberrations.

The requirements that we aimed to test for were with regard to the mirror segment piston, tip, and tilt wavefront motion, as well as measuring the precision and stability of the wavefront. As stated in McLeod et al. (2021), the relevant requirements are wavefront precision of $\leq$ 20nm RMS in all controlled modes, and wavefront stability of $\leq$ 20nm RMS over any five minute period where no changes are commanded by the user. The final WFPT design needs to generate $\geq 10\mu$m of wavefront piston displacement between segments, as well as $\geq 40\mu$m of tip and tilt between segments, both in the pupil and at the M2 conjugate location (McLeod et al. 2021). The full PTT mirror array, and its piezo-actuated two-segment prototype, have been designed in accordance with these standards. The simplified PTT array (see Section 2.2 and Figures 2.8, 2.9) is constructed using a linear translation stage with 25.4 mm of possible piston displacement ($\gg 10\mu$m). Using the ThorLabs KS05 mounts, the simplified PTT array can produce 40μm of tip-tilt wavefront displacement with a rotation of 6.3mrad, which is approximately one-half of a full rotation (1 revolution = 13.4mrad) of the hex-key-controlled mount screws. Therefore the simplified PTT array satisfies the requirements for producing sufficient wavefront segment differences. The current setup, with a piston-precision of 63 nm, does not offer wavefront precision of $\leq$ 20nm, but upcoming tests with the piezo-actuated PTT prototype may provide a lower uncertainty.

4.3 Future Work

Immediate next steps include additional testing of the piezo-actuated two-segment prototype of the full PTT array. This allows for precise control over the piston motion of the mirrors, as well as allowing us to measure the temporal stability on a setup that accurately represents the full seven-segment piezo-actuated PTT array. After these tests are complete ,the seven-segment array will be assembled and tested similarly.
Additionally, the OAPs intended to be used in the full WFPT will be obtained soon and polished on the back side to provide a reflective surface as required by the alignment procedure described in Section 3.3.2. The figure of these OAPs will be measured using the laser tracker and interferometer.
The full WFPT will combine the work presented in these disparate sections by using the SHWFS and DFS to measure the wavefront aberrations of a beam that has encountered two atmospheric turbulence phase plates, two segmented-PTT mirrors, and two deformable mirrors, guided by multiple pairs of aligned OAPs. By doing so, it will demonstrate that the AGWS system can take measurements with the required sensitivity, including all the major contributors to wavefront errors. The WFPT will first be tested with the same DFS prototype and SHWFS used for this thesis, until the first AGWS probe is completed.

Chapter 5

Appendix

5.1 Abbreviations

AGWS - Acquisition, Guiding, and Wavefront Sensing Systems

AcO - Active optics

AO - Adaptive Optics

DFS - Dispersed Fringe Sensor

GLAO - Ground layer adaptive optics

GMT - Giant Magellan Telescope

IR - Infrared

LTAO - Laser tomography adaptive optics

LT - Laser tracker

NGSAO - Natural guide star adaptive optics

OAP - Off-axis parabolic mirror

PTT - Piston-tip-tilt

RMS - Root mean square

SHWFS - Shack-Hartmann Wavefront Sensor

SMR - Spherically Mounted Retroreflector

VI - Virtual Image

WFPT - Wide Field Phasing Testbed

5.2 DFS Accuracy Results

Images	**Measured (μm)**	**Calculated (μm)**	**Measured - calculated**
1-2	5.0	8.83	-3.83
2-3	10.0	9.08	0.92
3-4	10.0	9.24	0.76
4-5	10.0	9.72	0.28

Table 5.1:: Batch 1 of results of testing the dispersed fringe sensor, using the two facet PTT array. Data obtained in November 2020 using an exposure time of 1100 ms and the Ninox camera.

Images	**Measured (μm)**	**Calculated (μm)**	**Measured - calculated**
1-3	5	1.37	3.63
2-3	5	1.57	3.43
3-4	5	7.26	-2.26
4-5	10	8.91	1.09
5-6	20	15.89	4.11
6-7	5	3.13	1.87
7-8	5	7.76	-2.76
8-9	5	6.72	-1.72
9-10	5	3.99	1.01

Table 5.2:: Batch 2 of results from testing the dispersed fringe sensor using the simplified two facet PTT array. Data obtained in February 2021 using an exposure time of 1100 ms and the Ninox camera.

Images	**Measured (μm)**	**Calculated (μm)**	**Measured - calculated**
1-2	1	1.16	-0.16
2-3	1	4.06	-3.06
3-4	2	4.06	-2.06
4-5	2	2.64	-0.64
5-6	1	1.86	-0.86
6-7	1	2.28	-1.28
7-8	2	3.01	-1.01

Table 5.3:: Batch 3 of results of testing the dispersed fringe sensor using the simplified two facet PTT array. Data obtained with an exposure time of 1100ms in February 2021 using the Ninox camera.

5.3 Laser Tracker Results

Table 5.4:: Repeated Measurements with Laser Tracker

Measurement number	3D Distance (μm) between Virtual Image ideal and measured positions	Measured Normal Vector (Bench coordinates)	θ_{between} (arcmin)
1	378 ±83	[-0.996164392, -0.0875013904, 9.90931191e-05]	1.24
2	396 ±83	[-0.996165289, -0.0874911989, 8.53426073e-05]	1.19
3	360 ±83	[-0.996168995, -0.0874489649, 1.11482383e-04]	1.08
4	372 ±83	[-0.996176482, -0.0873634904, 1.91472460e-04]	0.97
5	394 ±83	[-0.996159201, -0.0875605285, 1.48746689e-05]	1.41
7	401±83	[-0.996175822, -0.0873712270, 3.59573611e-05]	1.39
8	345 ±83	[-0.996164574, -0.0874991285, -2.07710261e-04]	0.75
9	411 ±83	[-0.996148534, -0.0876817087, 1.25237283e-04]	1.38

No adjustments to the setup were made between measurement sets. The mirror normal vector to which these values are compared is $\vec{N}_{\text{fiducial}}$=[-0.9961947, -0.08715574, 0]. Positions are measured in reflection off a flat mirror. Uncertainty on 3D distance measurement computed from the uncertainties on the real SMR position and the position of the virtual image.

References

4DTechnology. 2017, PhaseCam 6000 Data Sheet, Sales Brochure

4DTechnology. 2021, What is a Twyman-Green Interferometer?, Website, https://www.4dtechnology.com/products/twyman-green-interferometers/twyman-green-interferometer/

Babcock, H. W. 1953, PASP, 65, 229

Fanson, J., Bernstein, R., Angeli, G., et al. 2020, in Society of Photo-Optical Instrumentation Engineers (SPIE) Conference Series, Vol. 11445, Society of Photo-Optical Instrumentation Engineers (SPIE) Conference Series, 114451F

Finger, G., Baker, I., Alvarez, D., et al. 2012, in Society of Photo-Optical Instrumentation Engineers (SPIE) Conference Series, Vol. 8453, High Energy, Optical, and Infrared Detectors for Astronomy V, ed. A. D. Holland & J. W. Beletic, 84530T

Frostig, D. 2018, A Dispersed Fringe Sensor Prototype for the Giant Magellan Telescope, Senior Thesis, Harvard College

Goodman, J. W. 1996, Introduction to Fourier Optics, 2nd edn. (McGraw-Hill)

Hexagon. 2013, Leica Absolute Tracker AT402 Product Brochure, Sales Brochure

Kansky, J., McLeod, B., McMuldroch, S., & Podgorski, W. 2020, AGWS Software Preliminary Design, Giant Magellan Telescope Organization

Kopon, D., McLeod, B., Bouchez, A., et al. 2018, in Society of Photo-Optical Instrumentation Engineers (SPIE) Conference Series, Vol. 10703, Adaptive Optics Systems VI, ed. L. M. Close, L. Schreiber, & D. Schmidt, 107030X

McLeod, B., Bouchez, A., Catropa, D., et al. 2021, Wide Field Phasing Testbed Design, 4th edn., Smithsonian Astrophysical Observatory

Mueller, M., Szentgyorgyi, A., Baldwin, D., et al. 2018, in Society of Photo-Optical Instrumentation Engineers (SPIE) Conference Series, Vol. 10702, Ground-based and Airborne Instrumentation for Astronomy VII, ed. C. J. Evans, L. Simard, & H. Takami, 107029U

Pak, S., DePoy, D. L., Marshall, J. L., et al. 2020, in Society of Photo-Optical Instrumentation Engineers (SPIE) Conference Series, Vol. 11203, Advances in Optical

Astronomical Instrumentation 2019, 1120308

Pernechele, C., Bortoletto, F., Fantinel, D., & Giro, E. 2000, PASP, 112, 996

Platt, B., & Shack, R. 2001, Journal of Refractive Surgery

Science Advisory Committee, G., & Project Office, G. 2018, Giant Magellan Telescope Science Book 2018 (GMTO)

van Dam, M. A., McLeod, B. A., & Bouchez, A. H. 2016, Appl. Opt., 55, 539

Woods, D. F. 2009, PhD thesis, Harvard University

Wyant, J. C. 2016, Introduction to Interferometric Optical Testing, Presentation